



# The Space–Time Conservation Element and Solution Element Method—A New High–Resolution and Genuinely Multidimensional Paradigm for Solving Conservation Laws

## II. Numerical Simulation of Shock Waves and Contact Discontinuities

Xiao-Yen Wang  
University of Minnesota, Minneapolis, Minnesota

Chuen-Yen Chow  
University of Colorado at Boulder, Boulder, Colorado

Sin-Chung Chang  
Lewis Research Center, Cleveland, Ohio

## The NASA STI Program Office . . . in Profile

Since its founding, NASA has been dedicated to the advancement of aeronautics and space science. The NASA Scientific and Technical Information (STI) Program Office plays a key part in helping NASA maintain this important role.

The NASA STI Program Office is operated by Langley Research Center, the Lead Center for NASA's scientific and technical information. The NASA STI Program Office provides access to the NASA STI Database, the largest collection of aeronautical and space science STI in the world. The Program Office is also NASA's institutional mechanism for disseminating the results of its research and development activities. These results are published by NASA in the NASA STI Report Series, which includes the following report types:

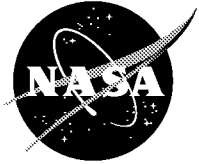
- TECHNICAL PUBLICATION. Reports of completed research or a major significant phase of research that present the results of NASA programs and include extensive data or theoretical analysis. Includes compilations of significant scientific and technical data and information deemed to be of continuing reference value. NASA's counterpart of peer-reviewed formal professional papers but has less stringent limitations on manuscript length and extent of graphic presentations.
- TECHNICAL MEMORANDUM. Scientific and technical findings that are preliminary or of specialized interest, e.g., quick release reports, working papers, and bibliographies that contain minimal annotation. Does not contain extensive analysis.
- CONTRACTOR REPORT. Scientific and technical findings by NASA-sponsored contractors and grantees.

- CONFERENCE PUBLICATION. Collected papers from scientific and technical conferences, symposia, seminars, or other meetings sponsored or cosponsored by NASA.
- SPECIAL PUBLICATION. Scientific, technical, or historical information from NASA programs, projects, and missions, often concerned with subjects having substantial public interest.
- TECHNICAL TRANSLATION. English-language translations of foreign scientific and technical material pertinent to NASA's mission.

Specialized services that complement the STI Program Office's diverse offerings include creating custom thesauri, building customized data bases, organizing and publishing research results . . . even providing videos.

For more information about the NASA STI Program Office, see the following:

- Access the NASA STI Program Home Page at <http://www.sti.nasa.gov>
- E-mail your question via the Internet to [help@sti.nasa.gov](mailto:help@sti.nasa.gov)
- Fax your question to the NASA Access Help Desk at (301) 621-0134
- Telephone the NASA Access Help Desk at (301) 621-0390
- Write to:  
NASA Access Help Desk  
NASA Center for AeroSpace Information  
7121 Standard Drive  
Hanover, MD 21076



# The Space–Time Conservation Element and Solution Element Method—A New High–Resolution and Genuinely Multidimensional Paradigm for Solving Conservation Laws

## II. Numerical Simulation of Shock Waves and Contact Discontinuities

Xiao-Yen Wang  
University of Minnesota, Minneapolis, Minnesota

Chuen-Yen Chow  
University of Colorado at Boulder, Boulder, Colorado

Sin-Chung Chang  
Lewis Research Center, Cleveland, Ohio

National Aeronautics and  
Space Administration

Lewis Research Center

Trade names or manufacturers' names are used in this report for identification only. This usage does not constitute an official endorsement, either expressed or implied, by the National Aeronautics and Space Administration.

Available from

NASA Center for Aerospace Information  
7121 Standard Drive  
Hanover, MD 21076  
Price Code: A04

National Technical Information Service  
5285 Port Royal Road  
Springfield, VA 22100  
Price Code: A04

**The Space-Time Conservation Element and Solution Element Method  
—A New High-Resolution and Genuinely Multidimensional Paradigm  
for Solving Conservation Laws**

**II. Numerical Simulation of Shock Waves and Contact Discontinuities**

**Xiao-Yen Wang**

**Department of Aerospace Engineering and Mechanics**

**University of Minnesota**

**Minneapolis, Minnesota 55455**

**e-mail: wangxy@aem.umn.edu**

**Chuen-Yen Chow**

**Department of Aerospace Engineering Sciences**

**University of Colorado at Boulder**

**Boulder, Colorado 80309-0429**

**e-mail: chow@astro.colorado.edu**

**and**

**Sin-Chung Chang**

**NASA Lewis Research Center**

**Cleveland, Ohio 44135**

**e-mail: sin-chung.chang@lerc.nasa.gov**

**web site: <http://www.lerc.nasa.gov/www/microbus>**

**Abstract**

Without resorting to special treatments for each individual test case, the 1D and 2D CE/SE shock-capturing schemes described in Part I [1] are used to simulate flows involving phenomena such as shock waves, contact discontinuities, expansion waves and their interactions. Five 1D and six 2D problems are considered to examine the capability and robustness of these schemes. Despite their simple logical structures and low computational cost (for the 2D CE/SE shock-capturing scheme, the CPU time is about 2  $\mu$ secs per mesh point per marching step on a Cray C90 machine), the numerical results, when compared with experimental data, exact solutions or numerical solutions by other methods, indicate that these schemes can accurately resolve shock and contact discontinuities consistently.

## 1. Introduction

The ability to generate finely resolved shocks and contact discontinuities at correct locations without introducing numerical oscillations is an important requirement of an accurate solver for high speed inviscid flows. Few established solvers (if indeed they exist) can meet this requirement consistently without resorting to special treatments (such as tuning some ad hoc parameters) for each individual case. The purpose of this paper is to show that, despite their simple logical structures and low computational cost, the 1D and 2D CE/SE shock-capturing schemes described in Part I [1] generally can meet the above requirement consistently with no special individual treatments required.

It was shown in [2] that the 1D CE/SE shock-capturing scheme is highly accurate in solving Sod's shock-tube problem. Recently, its accuracy in solving Harten's shock-tube problem was also evaluated against other schemes by Batten et al. [3]. They concluded that "The result (see Fig. 7) is quite remarkable, considering that the internal details of the Riemann fan are never used and, indeed, are never needed, because the entire Riemann fan is contained within the region of integration." In this paper, the accuracy of the present 1D scheme will be further evaluated using additional test problems. The results to be presented will further substantiate another conclusion reached in [3], i.e., "In fact, solutions produced with this scheme are broadly comparable to conventional MUSCL schemes ...."

As the first step, three standard test problems involving an infinitely long shock tube are used to evaluate the performance of the 1D CE/SE shock-capturing scheme. Flow phenomena associated with these test problems include shock waves, contact discontinuities, expansion fans and their interactions. In the second step, two test problems involving a shock tube with two closed ends are used to evaluate the capability of the 1D CE/SE shock-capturing scheme to simulate shock reflection accurately.

Finally, six 2D test problems are used to evaluate the performance of the 2D CE/SE shock-capturing scheme. The phenomena associated with these problems include complex shock-wave interactions, and multiple reflections of shock waves from solid bodies. One can conclude from the numerical results that the CE/SE method maintains its advantage over the traditional methods in simplicity, generality and accuracy even in a multidimensional space.

In the following sections, the boundary conditions used will be specified prior to the description of the numerical results. Note that the symbols and notations used in Part I [1] are inherited in Part II.

## 2. Boundary Conditions

### 2.1. Boundary Conditions for 1D Test Problems

Note that numerical simulations of the first three 1D test problems to be discussed in Sec. 3 are terminated before the region of nonuniform flow reaches the right and left boundaries of the computational domain. As a result, the boundary conditions used in these problems are immaterial as long as they are compatible with the uniform nature of the solution at each boundary. For simplicity, the steady-state boundary conditions are imposed at both boundaries. The solid-wall boundary conditions imposed at the closed ends of the shock tube involved in the last two 1D test problems are discussed here.

Consider Fig. 1. Let (i)  $x_j = x_0 - j\Delta x$  with  $x_0$  being a given constant and  $j$  a half or whole integer, (ii) the mesh point with  $j = n = 0$  not belong to the set  $\Omega$ , (iii)  $j_b > 0$  be a half or whole integer, and (iv) the right and left boundaries of the shock tube be located at  $x = x_{j_b}$  and  $x = x_{-j_b}$ , respectively. The solid-wall boundary conditions at each boundary will be constructed by assuming that, at any time  $t$ , the flow fields to the right and left of the boundary are the mirror images of each other. This assumption coupled with the definitions of  $u_1$ ,  $u_2$  and  $u_3$  given in Eq. (4.1) of [2] implies that, at any time  $t$  and for any  $x$ , (i)

$$u_m(x_{\pm j_b} - x, t) = u_m(x_{\pm j_b} + x, t) \quad \text{and} \quad \frac{\partial u_m}{\partial x}(x_{\pm j_b} - x, t) = -\frac{\partial u_m}{\partial x}(x_{\pm j_b} + x, t) \quad (2.1)$$

where  $m = 1, 3$ ; and (ii)

$$u_2(x_{\pm j_b} - x, t) = -u_2(x_{\pm j_b} + x, t) \quad \text{and} \quad \frac{\partial u_2}{\partial x}(x_{\pm j_b} - x, t) = \frac{\partial u_2}{\partial x}(x_{\pm j_b} + x, t) \quad (2.2)$$

Let (i)  $n = 1/2, 3/2, 5/2, \dots$  if  $j_b$  is a half integer; and (ii)  $n = 0, 1, 2, \dots$  if  $j_b$  is a whole integer. Then the numerical boundary conditions corresponding to Eqs. (2.1) and (2.2) are

$$(u_m)_{\pm j_b \pm 1/2}^n = (u_m)_{\pm j_b \mp 1/2}^n \quad \text{and} \quad (u_{m,r})_{\pm j_b \pm 1/2}^n = -(u_{m,r})_{\pm j_b \mp 1/2}^n, \quad m = 1, 3 \quad (2.3)$$

and

$$(u_2)_{\pm j_b \pm 1/2}^n = -(u_2)_{\pm j_b \mp 1/2}^n \quad \text{and} \quad (u_{2,r})_{\pm j_b \pm 1/2}^n = (u_{2,r})_{\pm j_b \mp 1/2}^n \quad (2.4)$$

respectively. Note that, according to Fig. 1, the boundary points  $(\pm j_b, n) \notin \Omega$  if  $n$  and  $j_b$  are related by either of the relations (i) and (ii) given preceding Eq. (2.3).

Let  $j_b$  be a half integer, then  $(\pm j_b, 0) \in \Omega$ . As a result, the initial data should be specified at the mesh points  $(j, 0)$ ,  $j = -j_b, -j_b - 1, \dots, j_b - 1, j_b$ . Note that the data must be consistent with the requirement that velocity vanishes at  $j = \pm j_b$ .

Let  $j_b$  be a whole integer, then  $(\pm j_b, 0) \notin \Omega$ . As a result, the initial data should be specified at the mesh points  $(j, 0)$ ,  $j = -j_b - 1/2, -j_b - 3/2, \dots, j_b - 3/2, j_b - 1/2$ .

Given the above initial data and the boundary conditions Eqs. (2.3) and (2.4), the marching variables at all  $(j, n) \in \Omega$  with  $j_b \leq j \leq -j_b$  and  $n \geq 0$  can be obtained by using the 1D CE/SE shock-capture scheme, i.e., Eqs. (2.32) and (2.65) of Part I [1].

## 2.2. Boundary Conditions for 2D Test Problems

The steady-state oblique shock problem suggested by Yee and others [4] is one of the 2D test problems to be discussed in Sec. 3. This test problem will be used as the prototypical case in the following discussion.

The computation domain and the shock locations ( $\overline{TE}$  and  $\overline{EF}$ ) are depicted in Fig. 2. The lower boundary is a solid-wall. Assuming  $\gamma = 1.4$ , the exact Euler solution to this problem is:

(a) In the region  $ABE$ ,

$$u = 2.9, \quad v = 0, \quad \rho = 1.0, \quad p = 1.0/1.4 \quad (2.5)$$

(b) In the region  $AFFD$ ,

$$u = 2.6193, \quad v = -0.50632, \quad \rho = 1.7000, \quad p = 1.5282 \quad (2.6)$$

(c) In the region  $ECCF$ ,

$$u = 2.4015, \quad v = 0, \quad \rho = 2.6872, \quad p = 2.9340 \quad (2.7)$$

The mesh used in the current numerical calculations is depicted in Fig. 3. Again a mesh point  $(j, k, n) \in \Omega_1$  (i.e.,  $n = 1/2, 3/2, 5/2, \dots$ ) is marked by a solid circle; while a mesh point  $(j, k, n) \in \Omega_2$  (i.e.,  $n = 0, 1, 2, \dots$ ) is marked by a hollow circle. The mesh is a special case ( $b = 0$ ) of that depicted in Figs. 5–9 in Part I [1]. Note that only the mesh points  $\in \Omega_2$  are present at the inflow and outflow boundaries. Moreover, a mesh point and the corresponding marching variable will be identified by the time-level number  $n$ , and two new mesh indices  $r$  and  $s$  which are given in Fig. 3 as a pair of integers enclosed in parentheses. Note that, for the mesh points  $\in \Omega_1$ ,  $r = 1, 2, 3, \dots, R, R - 1$ , and  $s = 2, 4, 6, \dots, 2S$ . On the other hand, for the mesh points  $\in \Omega_2$ ,  $r = 1, 2, 3, \dots, R, R - 1$ , and  $s = 1, 3, 5, \dots, 2S - 1, 2S - 1$ .

With the above preliminaries, the initial and boundary conditions can now be specified. At all mesh points  $(r, s, 0)$ , it is assumed that (i)  $u_m$ ,  $m = 1, 2, 3, 4$  are evaluated using Eq. (2.5), and (ii)

$$u_{m\zeta}^+ = u_{m\eta}^+ = 0, \quad m = 1, 2, 3, 4 \quad (2.8)$$

Furthermore, for  $n = 1, 2, 3, \dots$ , the above conditions (i) and (ii) are applied at all mesh points at the inflow boundary  $\overline{AB}$  (see Fig. 3).

At the upper boundary  $\overline{AD}$ , for all  $n = 1/2, 1, 3/2, 2, \dots$ , (i)  $u_m$  are evaluated using Eq. (2.6), and (ii)  $u_{m\zeta}^+$  and  $u_{m\eta}^+$  are evaluated using Eq. (2.8).

The solid-wall boundary conditions at  $\overline{BC}$  will be constructed by assuming that, at any time  $t$ , the flow fields below and above  $\overline{BC}$  are the mirror images of each other. By using the definitions of  $u_m$ ,  $m = 1, 2, 3, 4$ , given in Eq. (6.1) of Part I [1] and the fact that  $y = 0$  at any point on  $\overline{BC}$ , it can be shown that the last assumption implies that

$$u_m(x, -y, t) = u_m(x, y, t), \quad m = 1, 2, 4, \quad \text{and} \quad u_3(x, -y, t) = -u_3(x, y, t) \quad (2.9)$$

$$\frac{\partial u_m}{\partial x}(x, -y, t) = \frac{\partial u_m}{\partial x}(x, y, t) \quad \text{and} \quad \frac{\partial u_m}{\partial y}(x, -y, t) = -\frac{\partial u_m}{\partial y}(x, y, t), \quad m = 1, 2, 4 \quad (2.10)$$

and

$$\frac{\partial u_3}{\partial x}(x, -y, t) = -\frac{\partial u_3}{\partial x}(x, y, t) \quad \text{and} \quad \frac{\partial u_3}{\partial y}(x, -y, t) = \frac{\partial u_3}{\partial y}(x, y, t) \quad (2.11)$$

Consider the mesh depicted in Fig. 3. Then the numerical boundary conditions corresponding to Eqs. (2.9)–(2.11) are

$$(u_m)_{R+1,s}^n = (u_m)_{R,s}^n, \quad m = 1, 2, 4, \quad \text{and} \quad (u_3)_{R+1,s}^n = -(u_3)_{R,s}^n \quad (2.12)$$

$$(u_{m,r})_{R+1,s}^n = (u_{m,r})_{R,s}^n \quad \text{and} \quad (u_{m,y})_{R+1,s}^n = -(u_{m,y})_{R,s}^n, \quad m = 1, 2, 4 \quad (2.13)$$

and

$$(u_{3,r})_{R+1,s}^n = -(u_{3,r})_{R,s}^n, \quad \text{and} \quad (u_{3,y})_{R+1,s}^n = (u_{3,y})_{R,s}^n \quad (2.14)$$

respectively. According to Fig. 3, the range of  $s$  in Eqs. (2.12)–(2.14) is dependent on the time level  $n$ . Let (i)  $S' = S$  if  $S$  is even; and (ii)  $S' = S - 1$  if  $S$  is odd. Then (i)  $s = 4, 8, 12, \dots, 2S'$  if  $n = 1/2, 3/2, \dots$ , and (ii)  $s = 1, 5, 9, \dots, 2S' - 1$  if  $n = 1, 2, \dots$ . Furthermore, by using Eq. (C.4) of Part I [1] with  $b = 0$ , it can be shown that Eqs. (2.13) and (2.14) are equivalent to

$$(u_{m,\zeta})_{R+1,s}^n = (u_{m,\eta})_{R,s}^n \quad \text{and} \quad (u_{m,\eta})_{R+1,s}^n = (u_{m,\zeta})_{R,s}^n, \quad m = 1, 2, 4 \quad (2.15)$$

and

$$(u_{3,\zeta})_{R+1,s}^n = -(u_{3,\eta})_{R,s}^n, \quad \text{and} \quad (u_{3,\eta})_{R+1,s}^n = -(u_{3,\zeta})_{R,s}^n \quad (2.16)$$

respectively. Equations (2.12), (2.15) and (2.16) are the boundary conditions at the lower wall (a solid-wall). In other words, the marching variables associated with the mesh points below the solid-wall will be determined using these equations.

At the outflow boundary  $\overline{CD}$ , for any  $n = 1, 2, 3, \dots$ , and  $r = 1, 2, 3, \dots, R$ , we assume that

$$(u_m)_{r,2S+1}^n = (u_m)_{r,2S}^{n-1/2}, \quad m = 1, 2, 3, 4 \quad (2.17)$$

$$(u_{m,r})_{r,2S+1}^n = 0, \quad m = 1, 2, 3, 4 \quad (2.18)$$

and

$$(u_{mp})_{r,2S+1}^n = (u_{mp})_{r,2S}^{n-1/2}, \quad m = 1, 2, 3, 4 \quad (2.19)$$

By using Eq. (C4) of Part I [1] with  $b = 0$ , it can be shown that Eqs. (2.18) and (2.19) are equivalent to

$$(u_{m\zeta})_{r,2S+1}^n = \frac{1}{2} (u_{m\zeta} - u_{m\eta})_{r,2S}^{n-1/2}, \quad m = 1, 2, 3, 4 \quad (2.20)$$

and

$$(u_{m\eta})_{r,2S+1}^n = \frac{1}{2} (u_{m\eta} - u_{m\zeta})_{r,2S}^{n-1/2}, \quad m = 1, 2, 3, 4 \quad (2.21)$$

Thus the marching variables at the outflow boundary will be determined using Eqs. (2.17), (2.20) and (2.21). Note that, according to the numerical results to be presented in Sec. 3, the outflow boundary conditions are non-reflecting in nature.

With the aid of the above initial and boundary conditions, the marching variables at any time level can be determined by using the 2D CE/SE shock-capturing scheme.

In the oblique shock problem described above, only a horizontal solid wall is present. In other 2D test problems to be described later, both horizontal and vertical solid-walls may be present. As will be shown immediately, imposing the solid-wall boundary conditions at a vertical wall over a uniform mesh similar to that depicted in Fig. 3 is slightly more complicated than that at a horizontal wall.

Consider the mesh depicted in Fig. 4(a). Let  $\overline{BC}$  and  $\overline{CD}$  be solid-walls. Note that, given any exterior mesh point  $(R = 1, s, n)$  that lies immediately below  $\overline{BC}$ , one can find an interior mesh point that lies at the same time level and also is the mirror image (relative to  $\overline{BC}$ ) of the exterior mesh point. As a result, the solid-wall boundary conditions Eqs. (2.12)–(2.14) can be imposed. Contrarily, given any exterior mesh point  $(r, 2S - 1, n), n = 0, 1, 2, \dots$  that lies immediately to the right of  $\overline{CD}$ , one can not find an interior mesh point that lies at the same time level and is the mirror image (relative to  $\overline{CD}$ ) of the exterior mesh point. As a result, the mirror image conditions for the vertical wall  $\overline{CD}$ , i.e.,

$$(u_m)_{r,2S+1}^n = (u_m)_{r,2S}^n, \quad m = 1, 3, 4, \quad \text{and} \quad (u_2)_{r,2S+1}^n = -(u_2)_{r,2S}^n \quad (2.22)$$

$$(u_{mr})_{r,2S+1}^n = -(u_{mr})_{r,2S}^n \quad \text{and} \quad (u_{mp})_{r,2S+1}^n = (u_{mp})_{r,2S}^n, \quad m = 1, 3, 4 \quad (2.23)$$

and

$$(u_{2r})_{r,2S+1}^n = (u_{2r})_{r,2S}^n \quad \text{and} \quad (u_{2p})_{r,2S+1}^n = -(u_{2p})_{r,2S}^n \quad (2.24)$$

can not be used directly as the solid-wall boundary conditions.

Two approaches can be used to overcome the above difficulty. In the first approach, the following approximate forms of Eqs. (2.22)–(2.24) are used as the solid-wall boundary conditions:

$$(u_m)_{r,2S+1}^n = (u'_m)_{r,2S}^n, \quad m = 1, 3, 4, \quad \text{and} \quad (u_2)_{r,2S+1}^n = -(u'_2)_{r,2S}^n \quad (2.25)$$

$$(u_{m,r})_{r,2S+1}^n = -(u_{m,r})_{r,2S}^{n-1/2} \quad \text{and} \quad (u_{m,y})_{r,2S+1}^n = (u_{m,y})_{r,2S}^{n-1/2}, \quad m = 1, 3, 4 \quad (2.26)$$

and

$$(u_{2,r})_{r,2S+1}^n = (u_{2,r})_{r,2S}^{n-1/2}, \quad \text{and} \quad (u_{2,y})_{r,2S+1}^n = -(u_{2,y})_{r,2S}^{n-1/2} \quad (2.27)$$

Here  $(u_m')_{r,2S}^n$ ,  $m = 1, 2, 3, 4$ , are evaluated using the known marching variables at the mesh point  $(r, 2S, n - 1/2)$  with the aid of the first-order Taylor's expansion.

In the second and generally more accurate approach, the present marching procedure is applied over a dual mesh. It was explained in Sec. 8 of Part I that a dual mesh can be considered as the combination of two staggered space-time meshes, i.e., mesh 1 (Fig. 4(a)) and mesh 2 (Fig. 4(b)). As shown in Fig. 4(b), a mesh point of mesh 2 is also identified by two spatial indices  $r$  and  $s$ , and the time-level number  $n$ . Furthermore, a mesh point  $(r, s, n)$  of mesh 2 is marked by (i) a solid triangle if  $n = 1/2, 3/2, 5/2, \dots$ , and (ii) a hollow triangle if  $n = 0, 1, 2, \dots$

Let (i)  $r$  and  $s$  be any pair of whole integers and  $n$  be any whole or half integer such that  $(r, s, n)$  represents a mesh point of mesh 1, and (ii)  $n' = n + 1/2$ . Then, according to Figs. 4(a) and 4(b),  $(r, s, n')$  represents a mesh point of mesh 2 at the  $n'$ th time level with its spatial location being identical to that of  $(r, s, n)$ . Furthermore, (i) for  $n = 0, 1, 2, \dots$ ,  $(r, 2S - 1, n)$  is a mesh point of mesh 1 while  $(r, 2S, n)$  is a mesh point of mesh 2, (ii) for  $n = 1/2, 3/2, 5/2, \dots$ ,  $(r, 2S - 1, n)$  is a mesh point of mesh 2 while  $(r, 2S, n)$  is a mesh point of mesh 1, and (iii) for  $n = 0, 1/2, 1, 3/2, \dots$ , the mesh points  $(r, 2S - 1, n)$  and  $(r, 2S, n)$  lie at the same time level and, relative to  $\overline{CD}$ , are mirror images of each other. As a result, the solid-wall boundary conditions at  $\overline{CD}$  can be imposed using Eqs. (2.22)–(2.24), with  $n = 0, 1/2, 1, 3/2, \dots$ . Note that the marching variables associated with meshes 1 and 2 are now coupled through these boundary conditions. Also note that the Eqs. (2.23), (2.24), (2.26) and (2.27) can easily be converted to the versions associated with the  $(\zeta, \eta)$  coordinates by using Eq. (C.4) of Part I [1] with  $b = 0$ .

Imposing the conditions Eqs. (2.22)–(2.24) directly requires the use of a dual mesh. As a result, it has the disadvantage of doubling computational cost. However, the extra cost no longer becomes an issue if the use of dual meshes is mandated by other considerations. As will be explained in future papers, this indeed is the case for many practical applications including those requiring the use of unstructured triangular meshes.

### 3. Numerical Results

#### 3.1. One-Dimensional Problems

As a preliminary, a subtlety related to the specification of numerical initial conditions will be discussed here. As an example, we consider a shock-tube problem defined by the conservation law Eq. (2.19) in Part I [1] and the exact initial conditions: at  $t = 0$ ,

$$u_m = u_m(x, 0) \stackrel{\text{def}}{=} \begin{cases} U_m^+, & \text{if } x < d \\ U_m^-, & \text{if } x > d \end{cases} \quad (3.1)$$

Here (i)  $u_m$ ,  $m = 1, 2, 3$ , are the flow variables that appear in the 1D Euler equations Eq. (2.18) of Part I [1], and (ii)  $U_m^+$  and  $U_m^-$  ( $U_m^+ \neq U_m^-$ ),  $m = 1, 2, 3$ , and  $d$  are given constants.

To proceed, consider a computational mesh (see Fig. 1) with the properties that (i)  $j_b$  is a whole number, and (ii) a mesh point  $(j, 0) \in \Omega$  if and only if  $j \in \{-1/2, -3/2, \dots, -(j_b - 1/2)\}$ . For each  $(j, 0) \in \Omega$ , the line segment joining the two space-time points  $(x_j + \Delta x/2, 0)$  is part of  $\text{SE}(j, 0)$ . As a result, the space-time fluxes passing through the above line segment can be evaluated using either the exact or numerical initial conditions. The resulting two values are identical if and only if

$$\int_{x_j - \Delta x/2}^{x_j + \Delta x/2} u_m^-(x, 0; j, 0) dx = \int_{x_j - \Delta x/2}^{x_j + \Delta x/2} u_m(x, 0) dx, \quad m = 1, 2, 3 \quad (3.2)$$

Because of its flux-based nature, accuracy of the CE/SE Method generally will suffer (particularly if the exact initial conditions are not continuous) if the numerical initial conditions specified does not satisfy Eq. (3.2).

Let  $d = x_{j_d}$ , with  $j_d \in \{0, -1, -2, \dots, -(j_b - 1)\}$ . Then  $(j_d, 0)$  is the mid-point of the line segment joining the mesh points  $(j_d - 1/2, 0) \in \Omega$ . As a result, Eq. (3.2) is satisfied if the numerical initial conditions are: (i)

$$(u_m)_j^0 = u_m(x_j, 0) = \begin{cases} U_m^+, & \text{if } j = j_d - 1/2, j_d - 3/2, \dots, j_b - 1/2 \\ U_m^-, & \text{if } j = j_d + 1/2, j_d + 3/2, \dots, -j_b + 1/2 \end{cases} \quad (3.3)$$

and (ii)

$$(u_{m,x})_j^0 = \frac{\partial u_m}{\partial x}(x_j, 0) = 0 \quad \text{for } j = -1/2, -3/2, \dots, -(j_b - 1/2) \quad (3.4)$$

Note that (i) with  $(u_m)_j^0$  being defined by Eq. (3.3), Eq. (3.2) is satisfied regardless what the values are assigned to  $(u_{m,x})_j^0$ , and (ii) the impact on numerical results as a result of replacing Eq. (3.4) with other choices for  $(u_{m,x})_j^0$  generally fades away quickly after a few time steps.

Let  $d = x_{j\delta}$ , with  $j_\delta \in \{-.1/2, .3/2, \dots, .(j_b - 1/2)\}$ . Then  $(j_\delta, 0)$  represents a mesh point in  $\Omega$ . Furthermore, according to Eq. (3.1),  $u_m$  and  $\partial u_m / \partial x$  are not defined at the location of this mesh point. As a result, the initial conditions Eqs. (3.3) and (3.4) are no longer applicable. However, it can be shown easily that Eq. (3.2) is satisfied if, for any  $j$  with  $(j, 0) \in \Omega$ , we have (i)

$$(u_m)_j^0 = \begin{cases} u_m(x_j, 0), & \text{if } j \neq j_\delta \\ (U_m^+ - U_m^-)/2, & \text{if } j = j_\delta \end{cases} \quad (3.5)$$

and (ii)

$$(u_{m\tau})_j^0 = 0 \quad (3.6)$$

Note that (i) with  $(u_m)_j^0$  being defined by Eq. (3.5), Eq. (3.2) is satisfied regardless what the values are assigned to  $(u_{m\tau})_j^0$ , and (ii) the impact on numerical results as a result of replacing Eq. (3.6) with other choices for  $(u_{m\tau})_j^0$  generally fades away quickly after a few time steps.

Next we will compare the total number of the space-time mesh points involved in a CE/SE simulation and that involved in a simulation using a typical regular-mesh scheme which requires only one marching step to advance by a time period  $\Delta t$ . Let (i)  $L$  be the spatial dimension of the computational domain, (ii)  $T$  be the total simulation time, and (iii)  $\ell_0$  and  $n_0$  be the whole integers with  $L = \ell_0 \Delta x$  and  $T = n_0 \Delta t$ . Then, for the staggered mesh under consideration ( $\ell_0 = 2j_b$  in this case), the total number of the space-time mesh points involved in a CE/SE simulation (excluding those that lie on the initial line and spatial boundaries) is  $(2\ell_0 - 1) \cdot n_0$ . On the other hand, the corresponding number for a regular-mesh scheme is  $(\ell_0 - 1) \cdot n_0$ , i.e., about one half of that involved in the CE/SE simulation. The difference is due to the fact that it requires two marching steps to advance over each time period  $\Delta t$  in the CE/SE method.

Furthermore, we shall assume in this section that (i)  $\rho$ ,  $u$ ,  $p$ ,  $c$ ,  $M_s$ , and  $\gamma (= 1.4)$  denote the mass density, velocity, static pressure, sonic speed, shock wave Mach number and specific heat ratio, respectively, and (ii)  $CFL$  denotes the maximum value of  $(|u| + c)\Delta t / \Delta x$  reached during a numerical simulation. Also, for each test problem, (i) a mesh similar to that depicted in Fig. 1 will be used in numerical simulation, and (ii) the exact solution (if it exists) will be plotted (as a solid line) along with the numerical solution in every figure.

Also, note that  $\alpha$  (see Eq. (2.65) in Part I [1]) is the only adjustable parameter in the 1D CE/SE shock-capturing scheme. Generally, numerical wiggles near a discontinuity are satisfactorily suppressed by setting  $\alpha = 1$ . However, in some cases, complete suppression may require the use of a larger value of  $\alpha$  (e.g.,  $\alpha = 2, 3$ ).

With the above preliminaries, the numerical results of five 1D test problems will be presented. The first three involve shock tubes of infinite length. They are selected to demonstrate the 1D CE/SE shock-capturing scheme's robust capability for capturing shock and contact discontinuities as well as for simulating expansion waves. The last two

test problems involve shock tubes with closed ends. They are selected to demonstrate that the present solver is an accurate tool to study the end effects of shock-tube flows.

### 3.1.1. Sjögreen Problem

This problem is taken from [5]. The initial conditions at  $t = 0$  are:

$$(\rho, p, u) = \begin{cases} (1.0, 0.4, -2.0), & \text{if } x \leq 0.5 \\ (1.0, 0.4, 2.0), & \text{if } x \geq 0.5 \end{cases} \quad (3.7)$$

The CE/SE solution at  $t = 0.1$  (Fig. 5) is generated assuming  $\alpha = 1$ ,  $x_{-j_0} = 0$ ,  $x_{j_0} = 1$ ,  $\ell_0 = 100$  (i.e.,  $\Delta x = 0.01$ ), and  $\Delta t = 0.002$  ( $CFL \approx 0.55$ ).

The initial velocity discontinuity causes two rarefaction waves to propagate in opposite directions, leaving in between a region of high vacuum. It was mentioned in [6] that several Godunov-type schemes failed in this problem due to extremely low pressure in the middle region. It can be seen that the present solution agrees very well with the exact solution, without showing negative pressure in the middle region. Its accuracy is comparable to that obtained by Xu *et al.* [6] using a gas-kinetic scheme with  $\ell_0 = 200$ .

### 3.1.2. Shu-Osher Problem

The interaction of a moving shock ( $M_s = 3$ ) with a sinusoidal density wave is examined in this problem [7]. The initial conditions at  $t = 0$  are:

$$(\rho, p, u) = \begin{cases} (3.857, 10.333, 2.629), & \text{if } x \leq -4 \\ (1 - 0.2 \sin 5x, 1.0, 0.0), & \text{if } x \geq -4 \end{cases} \quad (3.8)$$

The CE/SE solution at  $t = 1.8$  (Fig. 6) is generated assuming  $\alpha = 1$ ,  $x_{-j_0} = -5$ ,  $x_{j_0} = 5$ ,  $\ell_0 = 800$  (i.e.,  $\Delta x = 0.0125$ ) and  $\Delta t = 0.0015$  ( $CFL \approx 0.582$ ).

This problem does not have a known exact solution. Several upwind schemes have been used to solve this problem to compare their ability in resolving the peaks appearing in the solution [8]. The present solution is comparable to those obtained in [8] by using the TVD1 and TVD2 schemes with  $\ell_0 = 800$ .

### 3.1.3. Merging of Two Shock Waves

The phenomenon considered in this problem involves two shock waves propagating to the right in an infinitely long tube with a shock of  $M_s = 3$  behind a weaker shock of  $M_s = 1.5$  (pp. 131-134 of [9]). The initial conditions at  $t = 0$  are:

$$(\rho, p, u) = \begin{cases} (7.1823, 25.4016, 3.84265), & \text{if } x \leq -2.0 \\ (1.8621, 2.4583, 0.8216), & \text{if } -2.0 \leq x \leq 1.5 \\ (1.0, 1.0, 0.0), & \text{if } 1.5 \leq x \end{cases} \quad (3.9)$$

A CE/SE simulation is carried out assuming  $\alpha = 2$ ,  $x_{-j_0} = -3$ ,  $x_{j_0} = 5$ ,  $\ell_0 = 100$  (i.e.,  $\Delta x = 0.1$ ) and  $\Delta t = 0.0135$  ( $CFL \approx 0.82$ ). The numerical results at  $t = 0.675$ ,  $1.1205$  and  $1.62$ , shown in Figs. 7–9, respectively, agree very well with the exact solutions. The two shocks remain separated until  $t \approx 1.1205$ . After that, one shock catches up with another and they merge into a stronger shock. The latter propagates to the right at a higher speed, leaving behind it a contact surface and a left-moving expansion fan (see Fig. 9).

Note that there is a small pressure overshoot near the shock in Fig. 9. As shown in Fig. 10, practically identical numerical results at  $t = 1.62$  are obtained if  $\alpha = 2$  is replaced by  $\alpha = 3$ . However, the overshoot is no longer present in Fig. 10.

### 3.1.4. Woodward-Colella Problem

This problem, concerning the interaction of two blast waves in a tube with closed ends, was proposed by Woodward and Colella [10]. It has no known exact solution. The initial conditions at  $t = 0$  are:

$$(\rho, p, u) = \begin{cases} (1.0, 1000, 0), & \text{if } x < 0.1 \\ (1.0, 0.01, 0), & \text{if } 0.1 \leq x \leq 0.9 \\ (1.0, 100, 0), & \text{if } 0.9 < x \end{cases} \quad (3.10)$$

The two ends are, respectively, at  $x = 0$  and  $x = 1$  where the reflecting boundary conditions are imposed.

The CE/SE solution at  $t = 0.038$  (Fig. 11) is generated assuming  $\alpha = 1$ ,  $\ell_0 = 800$  (i.e.,  $\Delta x = 0.00125$ ) and  $\Delta t = 1.25 \times 10^{-5}$  ( $CFL \approx 0.3524$ ). The flow field at  $t = 0.038$  (containing three contact surfaces and two shock waves) shows that the contact surfaces are more smeared than the shock discontinuities. The current numerical results are at least as accurate as those [11] generated by using the AUSM<sup>+</sup>, Roe, Van Leer, AUSMDV and AUSM<sup>+-w</sup> splitting schemes (see Fig. 12).

### 3.1.5. Waves in a Shock Tube with Closed Ends

The flow phenomena studied by this problem (see Fig. 13) include (i) the reflection of a shock wave and an expansion wave, and (ii) the interaction of the reflected waves and contact surface. The tube has closed ends at  $x = 0$  and  $x = 1$ , respectively. At  $t = 0$ , a diaphragm located at  $x = 0.25$  separating two gases at different conditions is burst (pp. 205–208 of [9]). With the initial conditions

$$(\rho, p, u) = \begin{cases} (20.0, 20.0, 0.0), & \text{if } x < 0.25 \\ (1.0, 1.0, 0.0), & \text{if } x > 0.25 \end{cases} \quad (3.11)$$

the breaking of the diaphragm creates a shock wave and an expansion wave separated by a contact surface.

To demonstrate the present solver's capability to maintain its accuracy after a long running time, the present simulation with  $\alpha = 2$ ,  $\Delta x = 0.01$  and  $\Delta t = 0.003$  is carried out for a period that is long enough to show successive reflections and interactions of shock waves, expansion waves and contact surfaces. When  $t = 0.09$ , the waves have not yet reached the ends as shown in Fig. 14. When  $t = 0.3$ , the left-moving expansion waves have been reflected from the left end while the shock wave is still moving to the right (see Fig. 15). At  $t = 0.4$ , the shock wave has already completed its reflection from the right end and the reflected shock wave is moving to the left (see Fig. 16). This reflected shock interacts with the right-moving contact surface to create a left-moving transmitted shock, a right-moving contact surface, and a right-moving shock wave that, when reaching the right end, is reflected again. At  $t = 0.585$ , there exist in the flow field two shock waves, one contact surface, and a region of expansion waves (see Fig. 17). Numerical results plotted in Fig. 14–17 correctly display the flow phenomena described in Fig. 13 at the four designated time instants.

### 3.2. Two-Dimensional Problems

In this part, six problems involving shock reflection, diffraction, and interaction are solved using the 2D CE/SE shock-capturing scheme. The first is a steady-state problem while the rest are time-dependent. A steady-state solution is obtained as the converged solution of the time-marching procedure [12]. Numerical results are compared with the exact solutions, experimental data or numerical solutions obtained by using other methods. In all of the following numerical simulations,  $\alpha = 2$  is assumed throughout the entire computational domain. Because  $\alpha$  is the only adjustable parameter in the present scheme (see Sec. 6 in Part I [1]), the same scheme is applied at all interior mesh points regardless of the presence of slow discontinuities. Also the approximate reflecting boundary conditions, which were discussed in Sec. 2 and can be implemented without using a dual mesh, will be imposed on a vertical solid-wall boundary unless specified otherwise.

To pave the way for the following presentation, a further discussion of the space-time mesh depicted in Fig. 3 is in order. According to Fig. 3, at each time level  $n = 0, 1, 2, \dots$ , there are  $S - 1$  staggered columns of mesh points (marked by hollow circles) with each column containing  $R - 1$  mesh points. Thus there are  $(S - 1) \times (R - 1)$  mesh points at each of these time levels. Furthermore, because two neighboring columns are separated by a distance  $w$  while two neighboring mesh points in any column are separated by a distance  $2h$ , we have  $S = W/w$  and  $R = H/(2h)$  where  $W$  and  $H$  are the width and height of the computational domain, respectively. If the first, the third, the fifth, ... columns were moved upward a distance  $h$ , then the mesh points marked by hollow circles form a regular Cartesian spatial mesh with  $S$  and  $R$  mesh intervals in the  $x$ - and  $y$ - directions, respectively. As a result, the mesh formed by the mesh points marked by hollow circles will be referred to as a  $S \times R$  mesh.

Similarly, at each time level  $n = 1/2, 3/2, \dots$ , there are  $S$  staggered columns of mesh points (marked by solid circles) with each column containing  $R - 1$  mesh points. Again two neighboring columns are separated by a distance  $w$  and two neighboring mesh points in

any column are separated by a distance  $2h$ . In this paper, the mesh formed by these mesh points will also be referred to as a  $S \times R$  mesh. In general, regardless of how its columns of mesh points are positioned, a spatial mesh covering a rectangular computational domain of width  $W$  and height  $H$  will be referred to as a  $(W/w) \times (H/(2h))$  mesh if two neighboring columns of mesh points are separated by a distance  $w$  and two neighboring mesh points in any column are separated by a distance  $2h$ .

For a dual mesh referred to earlier, there are two set of mesh points at one time level. If each set forms a  $(W/w) \times (H/(2h))$  mesh, then the dual mesh will be referred to as a dual  $(W/w) \times (H/(2h))$  mesh.

From the above analysis and the fact that it requires two marching steps to advance by a time period  $\Delta t$  in the CE/SE method, the total number of space-time mesh points involved in a 2D CE/SE simulation is approximately equal to  $(2T/\Delta t) \times S \times R$ , i.e., about twice that of a 2D single-step regular-mesh simulation if each simulation uses a  $S \times R$  mesh and both have the same values of  $\Delta t$  and total simulation time  $T$ . Note that, in the special case that a dual  $S \times R$  mesh is used, the total number of mesh points involved in a CE/SE simulation is approximately equal to  $(4T/\Delta t) \times S \times R$ .

### 3.2.1. Oblique Shock Problem

The computational domain, mesh structure and initial/boundary conditions used in the current simulations of this problem were described in Sec. 2. A numerical simulation is carried out using a  $60 \times 20$  mesh with  $\Delta t = 0.01$ . The resulting steady-state pressure contours and the pressure coefficient  $C_p$  ( $= 2(p/p_\infty - 1)/(\gamma M_\infty^2)$  with  $M_\infty = 2.9$  and  $p_\infty = 1.0/1.4$  being the inflow Mach number and pressure, respectively) at  $y = 0.5$  are plotted in Fig. 18, where the solid line represents the exact solution. The improvement on shock resolution by using a finer  $120 \times 40$  mesh can be seen in Fig. 19. No numerical oscillations are detected near either the incident or the reflected shocks, and the computed  $C_p$  agrees very well with the exact solution.

### 3.2.2. 2D Supersonic Flow Past a Step

Consider the supersonic channel flow of  $M_s = 3.0$  past a step depicted in Fig. 20, which is a standard benchmark problem in the literature. The flow exhibits complicated phenomena such as Mach stem, slip surface, expansion fan, and their interactions and reflections. It was used to test Harten's TVD ULTIC scheme [13], Giannakouras and Karniadakis's spectral element-FCCT (flux-corrected transport) method [14], and Van Leer's ultimate conservative difference scheme [15]. It was also used by Woodward and Colella [10] to compare the accuracy of different numerical methods in handling a shock discontinuity.

Note that the upper corner of the step is the center of a rarefaction fan and hence is a singular point of the flow. According to Woodward and Colella [10], unless special numerical treatments are applied near the corner of the step, the computed solutions would be seriously affected by large numerical errors generated just in the neighborhood of this singular point. Specifically, these errors cause a boundary layer to form just above the step in the wind tunnel. A shock then interacts with this boundary layer, and the qualitative

nature of the flow in the tunnel is altered more or less dramatically, depending upon the difference scheme and the mesh used. It will be shown immediately that satisfactory numerical solutions can be obtained by the present scheme without employing special treatments at the upper corner of the step.

The mesh used in the current simulation is also depicted in Fig. 20. Note that no mesh point is placed at the singular point at the upper corner of the step. The initial conditions are set to be the free stream conditions. Furthermore, the constant free stream conditions are imposed at the inlet while the nonreflecting boundary conditions Eqs. (2.17), (2.20) and (2.21) are imposed at the exit. In addition, the reflecting (solid-wall) boundary conditions are imposed at all other boundaries.

To show the improvement in flow solutions with decreased mesh spacing, the density contours of the solutions obtained by the present solver with  $60 \times 20$ ,  $120 \times 40$  and  $240 \times 80$  meshes are shown respectively in Fig. 21. Note that the values of  $\Delta t$  used in the above computations are identical to those used in [10], i.e., 0.0075, 0.005 and 0.0025, respectively ( $CFL = 0.8$ ). From Fig. 21, it is seen that the Mach stem, triple point, slip surface, expansion fan at the corner, and the interaction between the reflected shock and the rarefaction waves are accurately simulated in the present solutions. Note that an alternate simulation in which the dual-mesh reflecting boundary conditions Eqs. (2.22)–(2.24) are imposed at the vertical step wall yields almost identical results.

### 3.2.3. Blast Wave Problem

A blast flow field generated at an open-ended cylindrical shock tube, which was described in the experiment by Schmidt and Duffy [16], has been studied by Wang et al. [17] using an axisymmetric version of the present solver. The cylindrical shock tube configuration and the initial conditions are depicted in Fig. 22. An unsteady flow field is created at  $t = 0$  by the sudden removal of a diaphragm at the lip of the tube, which separates a compressed fluid in region 2 inside the tube from the surrounding stagnant fluid in region 1. The direct contact of the high and low pressure regions results in a rarefaction wave propagating back into the tube and, in the meantime, a shock wave blasting away from the tube lip into the ambient open space. The comparison between experimental results and CE/SE solutions presented in [17] shows that the unsteady blast wave development was captured very well in the numerical solutions.

Consider the planar-flow version of the above problem where it is assumed that the configuration of the planar-flow version is such that its cross section is identical to that of the axisymmetric-flow version. In other words, the tube in the original problem is replaced by two slabs in its planar-flow version. A numerical simulation of the new version was carried out using the 2D CE/SE shock-capturing scheme. The computational domain is depicted in Fig. 23 with the understanding that the axis of symmetry is represented by the lower boundary. For illustrative purposes, some CE/SE mesh points are also shown schematically in the same figure.

The computation was performed over a  $160 \times 120$  mesh with  $\Delta t = 0.0025$ . The nonreflecting boundary conditions are imposed at the inlet and outlet, while the reflecting

boundary conditions are imposed at the lower and upper boundaries, and at all slab walls.

To show the time history of flow development, numerical solutions at eight time levels are shown in Figs. 24 and 25, in which the pressure and density contours ranging from 0 to 5.88 with a constant interval of 0.049 are plotted. The sequential plots reveal that as the blast wave initiated from the open end of the region between two slabs propagates to the right, a vortex is developed at the lip of the slab wall, and it moves downstream with an ascending motion. When the blast wave reaches the upper wall, it is reflected as shown in the plot at  $t = 1.0$  msec. In the meantime on the axis of symmetry a normal shock is formed ahead of the vortex and moves slowly in the downstream direction, while a jet shear layer is created at the lip of the region between two slabs. At  $t = 1.5$  msec, the portion of the blast wave that is reflected from the upper wall is shown to move toward the vortex. After passing the vortex, the blast wave becomes curved and keeps moving forward to interact with the normal shock below, as shown in the plots at  $t = 1.7$  msec. At  $t = 1.9$  msec, the flow pattern reveals that as a result of the interaction, the blast wave is broken into two parts while several new vortices are created. More complex flow patterns are shown at  $t = 2.1$  and 2.3 msec, describing further reflection and interaction of shock waves and vortices.

Despite the difference between planar and axisymmetric configurations, the computed flow fields agree extremely well with those shown in the shadowgraph pictures of the test results [16] taken at  $t = 0.1996$  and 0.4937 msec, respectively.

### 3.2.4. Diffraction of Shock Wave down a Step

Two experimental cases, described in [p. 148, 18], about the diffraction of a plane shock wave down a step, are simulated here. The computational domain ( $0 \leq x, y \leq 3.5$ ) is depicted in Fig. 26 with the upper boundary being a solid wall. The shock wave is located at the corner of the step at  $t = 0$ . The reflecting boundary conditions are imposed at the upper and lower walls as well as all step walls. The non-reflecting boundary conditions are imposed at the inlet and outlet. In the first case in which a weak shock wave with  $M_s = 1.3$  is considered, the numerical simulation is carried out using a  $140 \times 70$  mesh with  $\Delta t = 0.01$ . The computed solutions at  $t = 0.42$ , 1.12, and 1.82 are also shown in Fig. 26, in which the density contours are plotted from 0.8 to 1.55 with an interval of 0.025. A comparison of the computed solutions with the first set of the photographs shown on p.148 of [18] (reproduced here as Fig. 27) reveals that there is general agreement in flow pattern, except for those phenomena induced by the viscous effect. The observed shock waves, slip lines and vortices are very well captured in the numerical solutions.

In the second case in which a stronger shock wave with  $M_s = 2.4$  is considered, the numerical simulation is carried out using a  $180 \times 70$  mesh ( $0 \leq x \leq 4.5$  and  $0 \leq y \leq 3.5$ ) with  $\Delta t = 0.005$ . The computed solutions at  $t = 0.275$ , 0.875, and 1.375 are shown in Fig. 28, in which 30 density contours are plotted with the contour values increasing from the minimum of 0.5 with a constant interval of 0.095. The flow patterns exhibited in Fig. 28 are more complicated than those in Fig. 26. In large measure they are also similar

to those observed in the second set of the photographs shown on p.148 of [18] (reproduced here as Fig. 29).

### 3.2.5. Shock Reflection from a Dust Layer

Here a practical problem of shock reflection from a dust layer is studied. Following the wedge model described in [19], we consider a plane shock moving to the right with Mach number  $M_s = 1.41$  toward a wedge whose surface is inclined at angle  $\theta_w$ , as shown in Fig. 30. Square protuberances of size  $L/2$  are placed at equal distances  $L$  apart on the surface to simulate dust particles. The common origin of the two coordinate systems  $(x, y)$  and  $(x', y')$  is situated at the tip of the wedge, with the  $x'$  and  $y'$  axes being parallel and normal to the wedge surface, respectively.

As depicted in Fig. 31, the computational domain ( $-0.5 \leq x'/L \leq 7.0$  and  $0 \leq y'/L \leq 4$ ) contains seven protuberances. The front of the incident shock thus makes an angle  $\theta_w$  with the  $y'$  axis. At  $t = 0$ , the computational domain is divided into two flow regions by the shock front that intersects the  $x'$ -axis at  $x'/L = -0.4$ . Standard stationary atmospheric conditions are assumed in the region to the right of the shock front, while constant fluid conditions with  $M_s = 1.41$  are assumed in the other region. Reflecting boundary conditions are imposed at all solid walls, while non-reflecting boundary conditions are implemented at both the inlet and outlet, and on the part of  $x'$  axis with  $-0.5 \leq x'/L \leq 0$ , through which waves can move freely. On the upper boundary ( $y'/L = 4$ ), where the reflected waves have not reached before the end of all simulations, numerical values are assigned ahead of and behind the plane shock according to the exact solution. Computations were carried out for  $\theta_w = 20^\circ, 30^\circ$ , and  $40^\circ$ , respectively, using a  $300 \times 180$  mesh with  $\Delta t = 0.01$ , where  $t$  is made dimensionless using  $L$  as the reference length and the speed of sound in the undisturbed region as the reference speed.

In order to show a clear comparison between the experimental and computed results, the CE/SE solutions are plotted in the  $(x, y)$  coordinates through a coordinate transformation. First, to show the unsteady evolution of wave patterns resulting from the reflection of shock waves over the dusty wedge, computed density contours at four different time levels for  $\theta_w = 30^\circ$  are plotted in Fig. 32. The effect of varying wedge angle on wave pattern can be observed in the density contour plots shown in Fig. 33 for  $\theta_w = 20^\circ$  at  $t = 3.8$  and in Fig. 34 for  $\theta_w = 40^\circ$  at  $t = 3.0$ , when the incident shock wave is standing at the upper right corner of the 6th protuberance. The schlieren photographs taken from [19] are reproduced in Figs. 35–37 to show representative wave patterns for the cases  $\theta_w = 20^\circ, 30^\circ$  and  $40^\circ$  at different instants. In these photographs, (i) Model B and Model D represent the laboratory models with  $L = 8$  and  $2$  mm, respectively, and (iii)  $T_1$  denotes the triple point generated by the reflection of shock waves from the first protuberance. The location of  $T_1$  in the  $x$  direction is indicated by the numerical value of  $x/L$  in each figure. It is seen that, as the incident shock wave moves forward, a compression wave is reflected from each protuberance and an expansion wave is generated from its back. Gradually, the individual compression waves accumulate to form an envelope  $C_s$  and a stronger compression wave  $C'_s$  (see Fig. 36). For the cases with  $\theta_w = 20^\circ$  and  $\theta_w = 30^\circ$ , the developments of

wave patterns are almost the same, while for  $\theta_w = 40^\circ$ , a kink point  $K$  appears as shown in Fig. 37. A comparison between experimental and numerical results indicates that the photographed wave patterns are correctly captured in the CE/SE solutions. The close resemblance between Fig. 33 and Fig. 35 and that between Fig. 32(d) and Fig. 36 in terms of both wave and vortex structures are clearly recognizable.

### 3.2.6. Implosion/Explosion of Polygonal Shock Waves in a Box

The problem concerning the implosion/explosion of a polygonal shock wave in a square box studied in [20] is investigated here. Not only the early stage of the implosion/explosion process, but also its later development, which was not studied in [20], are simulated here. It further demonstrates the robustness of the current Euler scheme in its ability to model multiple shock reflections and interactions.

All simulations are carried out using (i) a dual  $240 \times 240$  mesh covering a square box ( $-2 \leq x, y \leq 2$ ), and (ii) a *CFL* number = 0.9. The reflecting boundary conditions are imposed at the four sides of the square box with the understanding that the more accurate dual-mesh reflecting boundary conditions Eqs. (2.22)–(2.24) are used at the vertical walls.

The initial shock wave configuration is a regular polygon. It is assumed that (i) the polygon shares with the square box the same geometric center (located at  $(0,0)$ ), (ii) one of the vertices of the polygon is located at  $(0, 0.8\sqrt{3})$ , and (iii) there is a low pressure region inside the polygon with a pressure ratio of 10 across the shock. Note that, as a result of (i) and (ii), the vertices of the polygon are points on the circumference of the circle that has a radius =  $0.8\sqrt{3}$  and is centered at  $(0,0)$ .

As the first step, the early flow field is studied for three cases in which the initial shock wave configurations are an equilateral triangle, a square and a regular pentagon, respectively. The computed pressure and density contour plots at different time levels are shown in Figs. 38 and 39. Wave patterns similar to those shown in Figs. 1–5 of [20], obtained using a TVD method on a  $359 \times 359$  mesh, are clearly observed in the CE/SE solutions, displaying detailed features such as Mach stems and polygon-shaped flow discontinuities.

As the second step, the implosion/explosion of a hexagonal shock wave is simulated until the second implosion of the shock wave is observed in the box. More complex flow phenomena can be seen in the pressure and density contour plots of Figs. 40 and 41, including the reflections of shock waves, shock-shock interaction, and shock-contact surface interaction. It is interesting to note that the shape of the contact surface centered at the center of the box remains unchanged even after the passage of shock waves. Further development of the implosion/explosion process can also be simulated using the same solver.

#### 4. Conclusions and Discussions

By comparing the current numerical results with experimental data, exact solutions or numerical solutions generated by other methods, it has been shown that the 1D and 2D CE/SE shock-capturing schemes can accurately resolve shock and contact discontinuities consistently. Furthermore, it has also been shown that the present schemes are genuinely robust, i.e., unlike many other shock-capturing schemes, their accuracy are achieved without resorting to special treatments for each individual case.

Because of their simple logical structures and totally explicit nature, the present schemes are also highly computational efficient. As an example, consider a vectorized code implementing the single-mesh 2D CE/SE shock-capturing scheme. For a  $300 \times 120$  mesh, the CPU time on a Cray C90 required to execute 180 marching steps ( $T = 180 \times (\Delta t/2)$ ) is only 14 seconds, i.e., about 2.16  $\mu$ secs per mesh point per marching step.

A disadvantage of the present schemes is that the total number of space-time mesh points involved in each single-mesh (dual-mesh) CE/SE simulation is about twice (four times) that of a typical single-step regular-mesh simulation if each simulation uses a  $S \times R$  mesh and both have the same values of  $S$ ,  $R$ ,  $\Delta t$  and total simulation time  $T$ . However, this disadvantage can be compensated for by other advantages the present scheme has, such as higher accuracy and lower computational cost per mesh point per marching step. As an example, consider the test problem discussed in Sec. 3.2.6. The TVD results given in [20] are generated using a  $359 \times 359$  mesh while the CE/SE results are generated using a dual  $240 \times 240$  mesh. Assuming that the same *CFL* number is used in both simulations, then the value of  $\Delta t$  used in the CE/SE simulation is  $359/240$  times that used in the TVD simulation. It can be shown easily that the total number of space-time mesh points involved in the CE/SE simulation is only about 20% more than that used in the TVD simulation. The slight disadvantage of the present scheme can be further compensated for not only by its possible lower computation cost per mesh point per marching step, but more importantly, by its ability to simulate the implosion/explosion process long past the early stage simulated by the TVD method.

## References

- [1] S.C. Chang, X.Y. Wang and C.Y. Chow, "The Space-Time Conservation Element and Solution Element Method—A New High-Resolution and Genuinely Multidimensional Paradigm for Solving Conservation Laws. I. The Two-Dimensional Time Marching Schemes," NASA TM 208843, December 1998.
- [2] S.C. Chang, "The Method of Space-Time Conservation Element and Solution Element – A New Approach for Solving the Navier-Stokes and Euler Equations," *J. Comput. Phys.* **119**, 295 (1995).
- [3] P. Batten, M.A. Leszcziner and U.C. Goldberg, "Average-State Jacobians and Implicit Methods for Compressible Viscous and Turbulent Flows," *J. Comp. Phys.* **137**, 38 (1997).
- [4] H.C. Yee, R.F. Warming and A. Harten, "Implicit Total Variation Diminishing (TVD) Schemes for Steady-State Calculations," AIAA paper 83-1902 (1983).
- [5] B. Einfeldt, C.D. Munz, P.L. Roe and B. Sjögren, "On Godunov-Type Methods near Low Densities," *J. Comput. Phys.* **92**, 273 (1991).
- [6] K. Xu, L. Martinelli and A. Jameson, "Gas-Kinetic Finite Volume Method, Flux-Vector Splitting and Artificial Diffusion," *J. Comput. Phys.* **120**, 48 (1995).
- [7] C.W. Shu and S. Osher, "Efficient Implementation of Essentially Non-Oscillatory Shock-Capturing Scheme, II," *J. Comput. Phys.* **88**, 32 (1989).
- [8] H.T. Huynh, "Accurate Upwind Schemes for the Euler Equations," AIAA paper 95-1737-CP (1995).
- [9] G. Rudegger, *Wave Diagrams for Nonsteady Flow in Ducts*. Van Nostrand, Princeton, NJ, 1955.
- [10] P. Woodward and P. Colella, "The Numerical Simulation of Two-Dimensional Fluid Flow with Strong Shock," *J. Comput. Phys.* **54**, 115 (1984).
- [11] M.S. Liou, "Progress Towards an Improved CFD Method: AUSM+," AIAA paper 95-1701-CP (1995).
- [12] S.C. Chang, C.Y. Wang and C.Y. Chow, "New Developments in the Method of Space-Time Conservation Element and Solution Element—Applications to Two-Dimensional Time-Marching Problems," NASA TM 106758, December 1994.
- [13] A. Harten, "High Resolution Schemes for Hyperbolic Conservation Laws," *J. Comput. Phys.* **49**, 357 (1983).
- [14] J. Giannakopoulos and G.E. Karniadakis, "A Spectral Element-FCT Method for the Compressible Euler Equations," *J. Comput. Phys.* **115**, 65 (1994).
- [15] B. van Leer, "Toward the Ultimate Conservative Difference Scheme. v. A Second-Order Sequel to Godunov's Method," *J. Comput. Phys.* **32**, 101 (1979).
- [16] E.M. Schmidt and S. Duffy, "Noise from Shock Tube Facilities," AIAA paper 85-0049 (1985).
- [17] X.Y. Wang, S.C. Chang and C.Y. Chow, "Application of the Method of Space-Time Conservation Element and Solution Element to Axisymmetric Euler Time-Marching problems," in *A Collection of Technical Papers, Vol. III, Sixth International Symposium on Computational Fluid Dynamics*, p. 1351, Lake Tahoe, Nevada, 1995.

- [18] M. Van Dyke, *An Album of Fluid Motion*, The Parabolic Press, Stanford, California, 1988.
- [19] T. Suzuki, T. Adachi and S. Kobayashi, "An Experimental Analysis on Shock Reflection over the Two-Dimensional Model of a Dust Layer," in *17th International Symposium on Shock Waves & Shock Tube*, edited by Yong W. Kim, Bethlehem, PA, 1989.
- [20] T. Aki and F. Higashino, "A Numerical Study on the Implosion of Polygonally Interacting Shocks and Consecutive Explosion in a Box," in *17th International Symposium on Shock Waves & Shock Tube*, edited by Yong W. Kim, Bethlehem, PA, 1989.

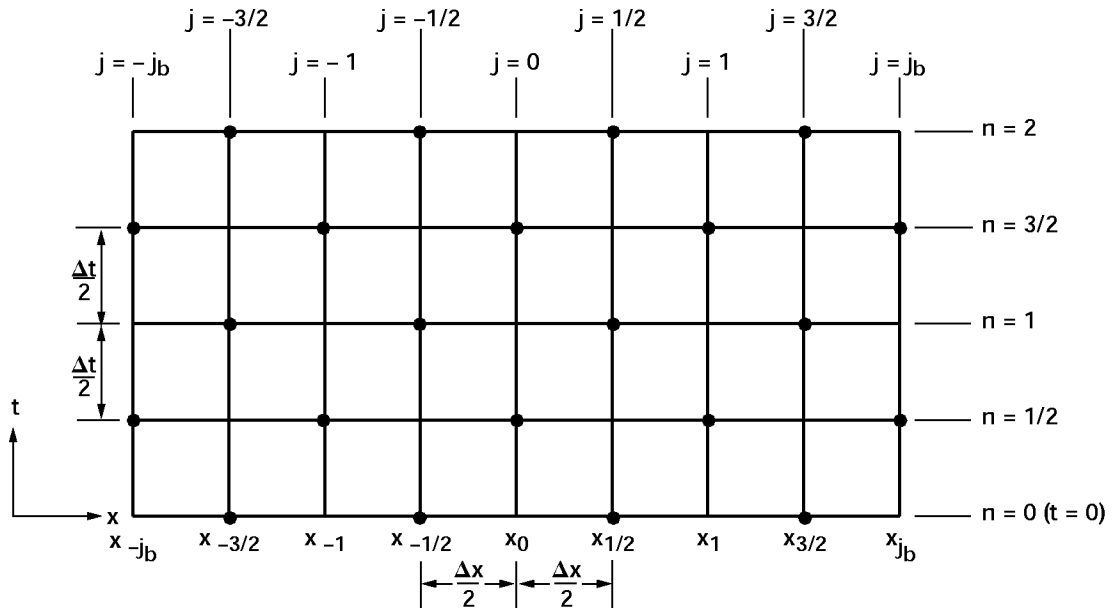


Figure 1: A staggered space-time mesh with the spatial boundaries at  $j = \pm j_b$  ( $j_b = 2$ ).

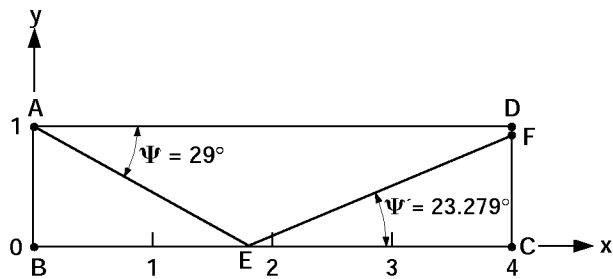


Figure 2: The computation domain and the shock locations of a steady-state oblique shock problem.

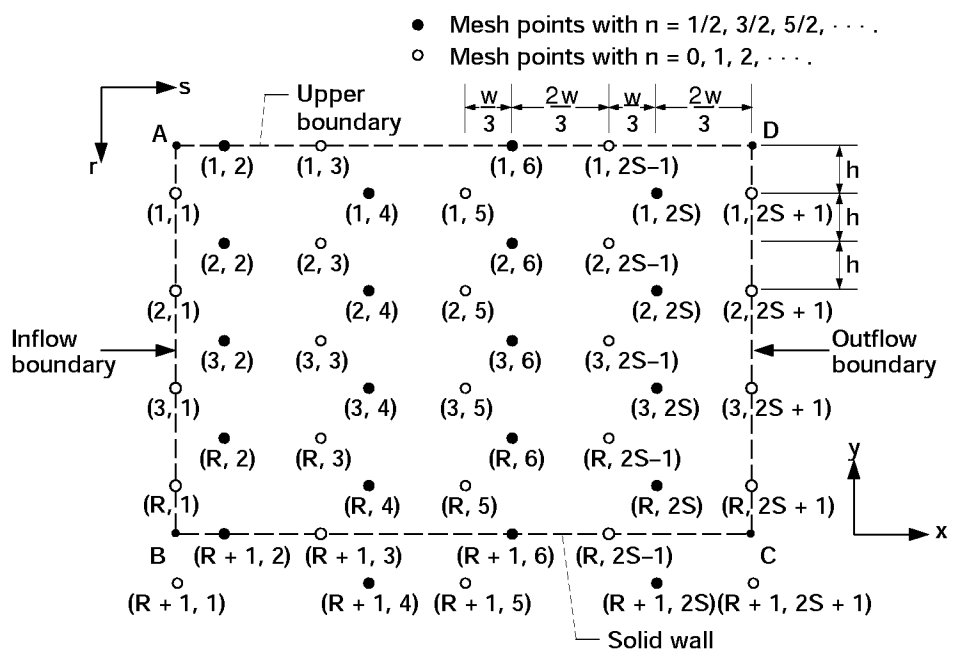


Figure 3: The spatial locations and the mesh indices ( $r, s$ ) of mesh points used in a steady-state oblique shock problem ( $R = S = 4$ ).

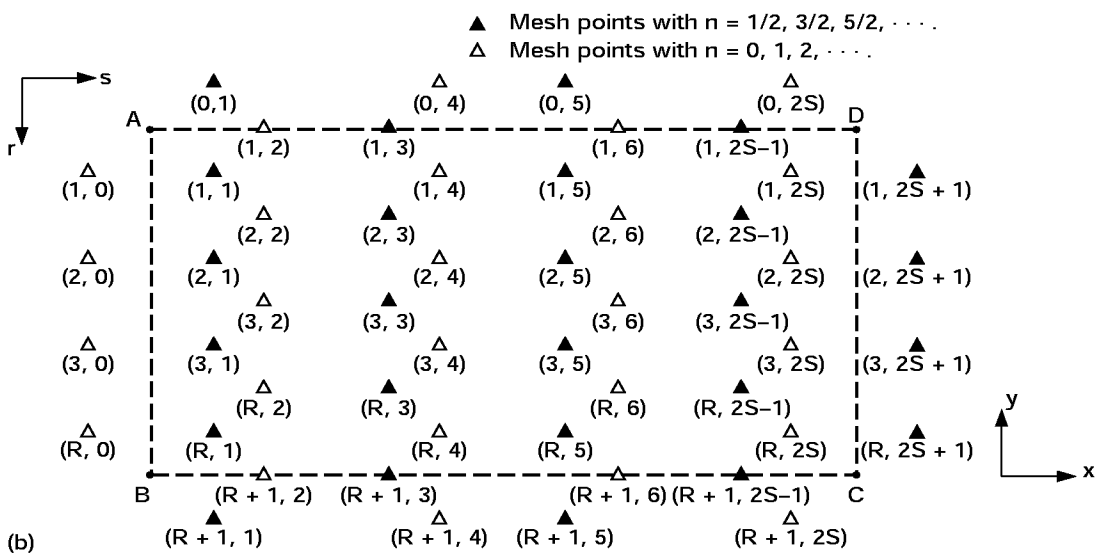
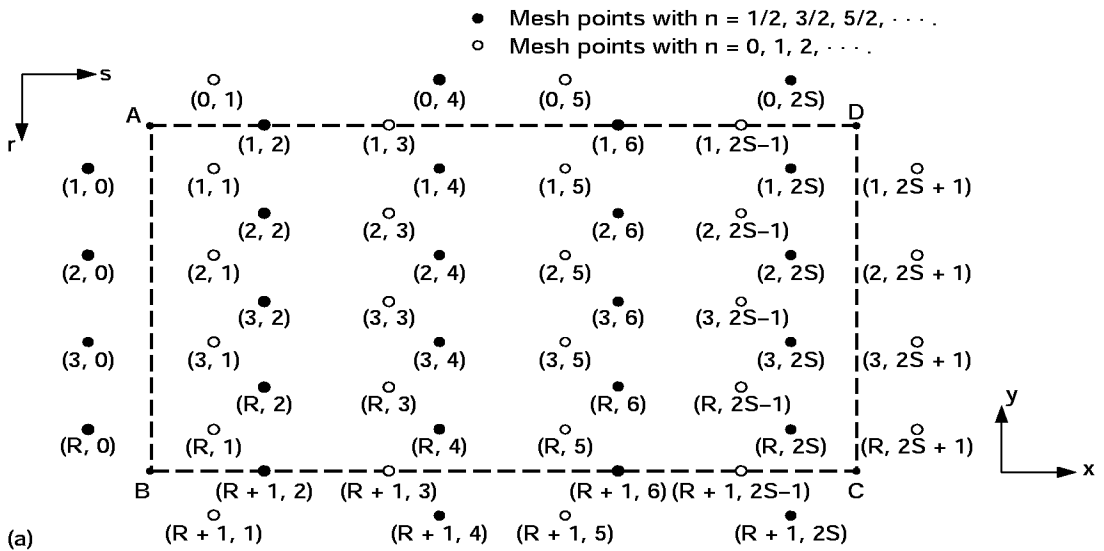


Figure 4: The spatial locations and the mesh indices ( $r, s$ ) of mesh points used in a problem with both horizontal and vertical walls. (a) Mesh 1. (b) Mesh 2.

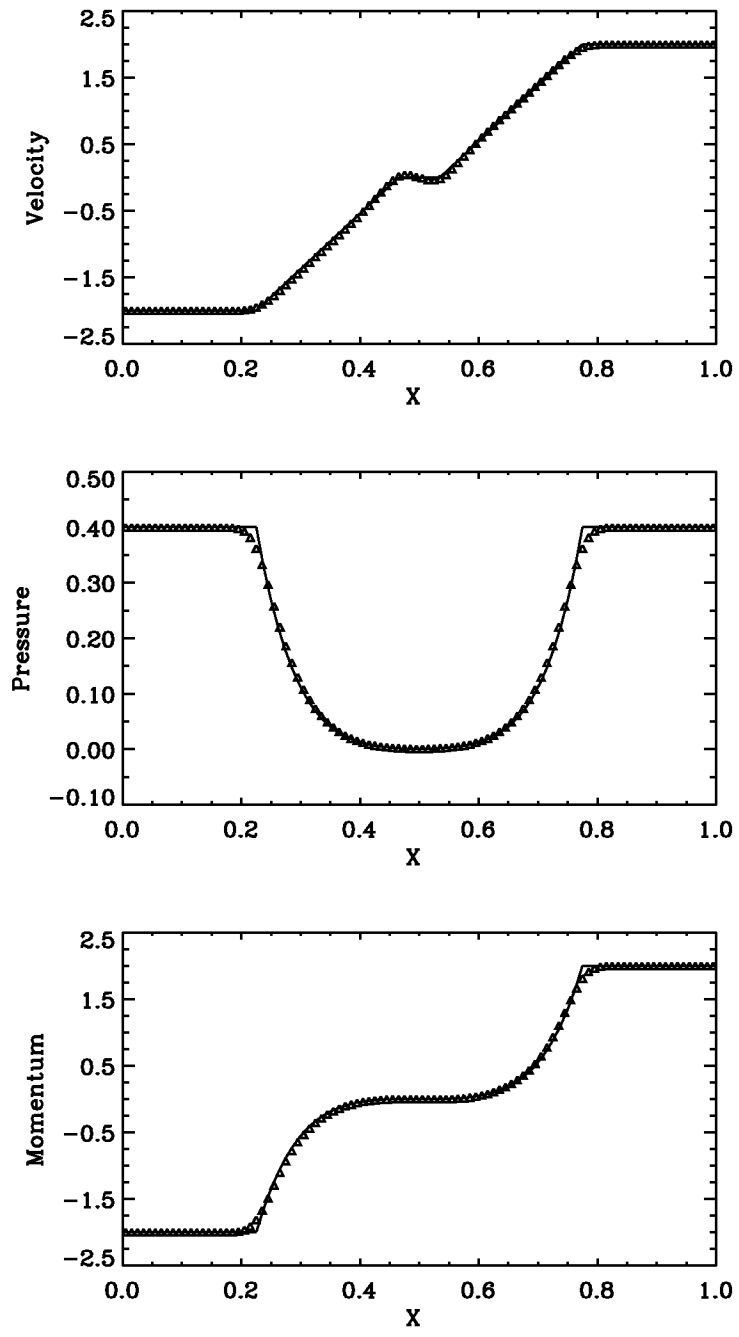


Figure 5: The CE/SE solution and the exact solution of the Sjögren problem.

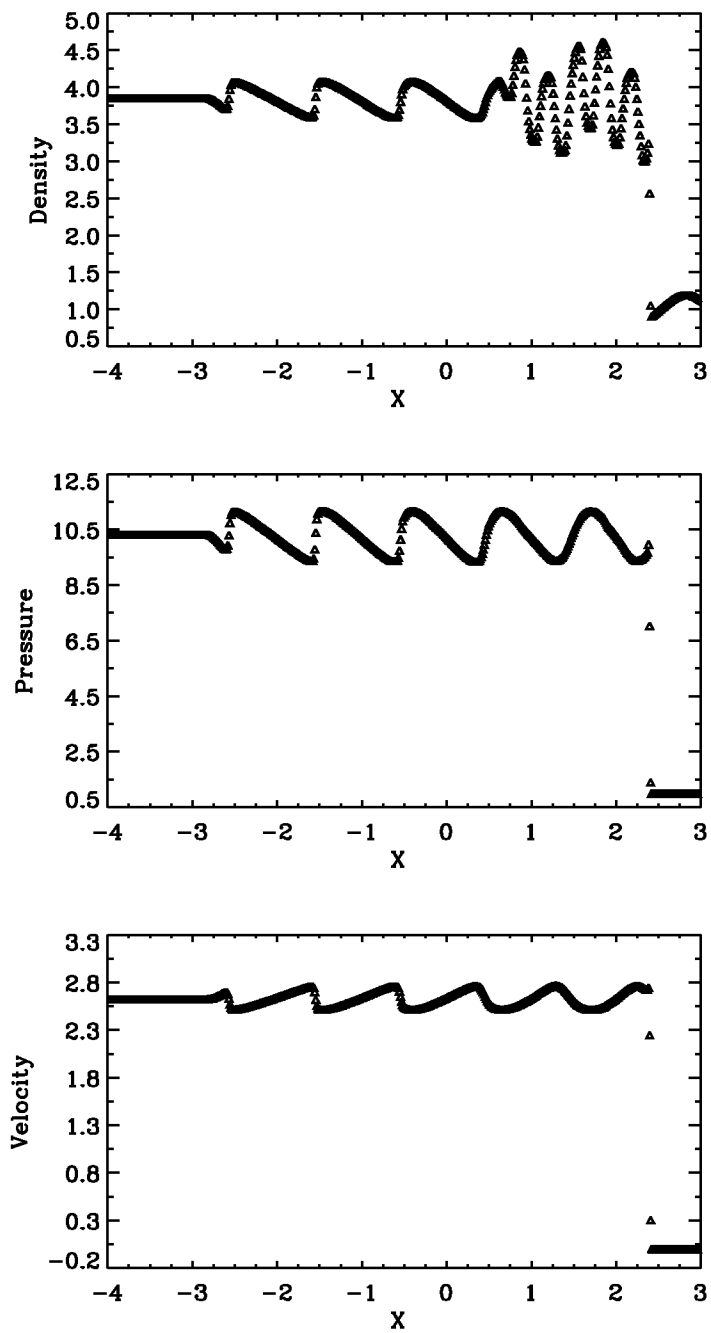


Figure 6: The CE/SE solution of the Shu-Osher problem.

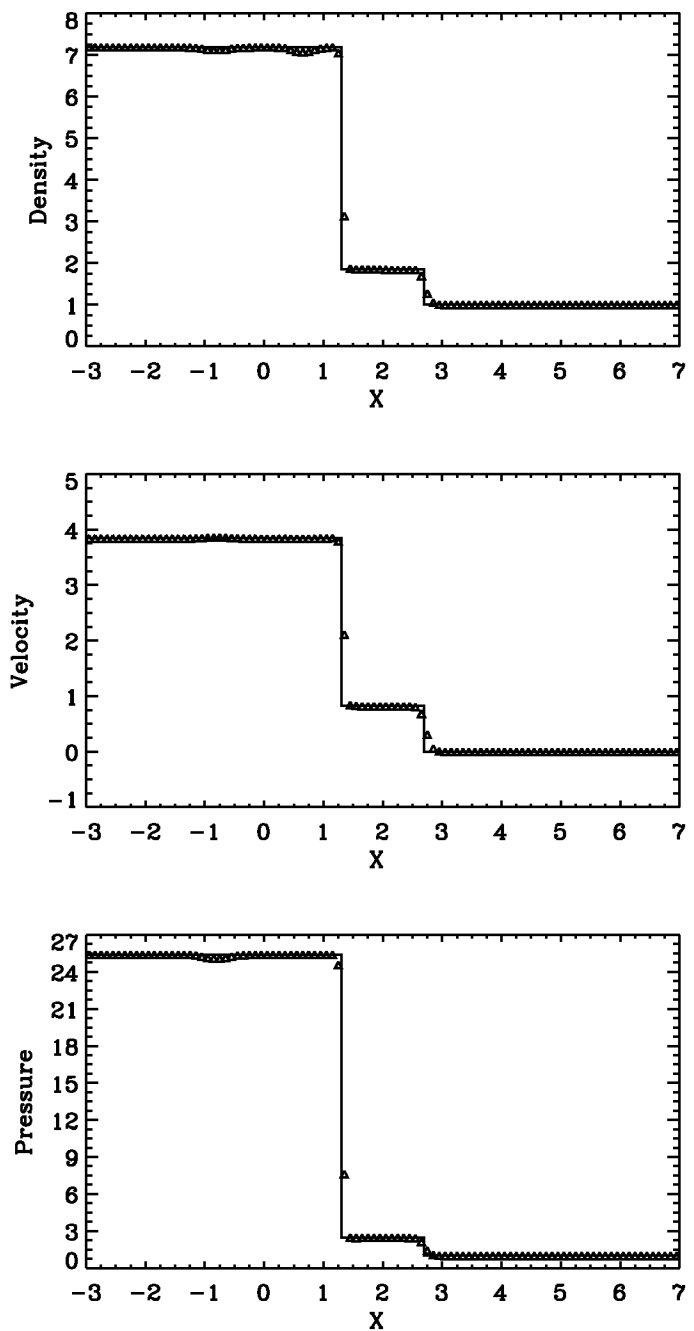


Figure 7: The CE/SE solution and the exact solution of the shock-wave merging problem ( $t = 0.675$ ,  $\alpha = 2$ ).

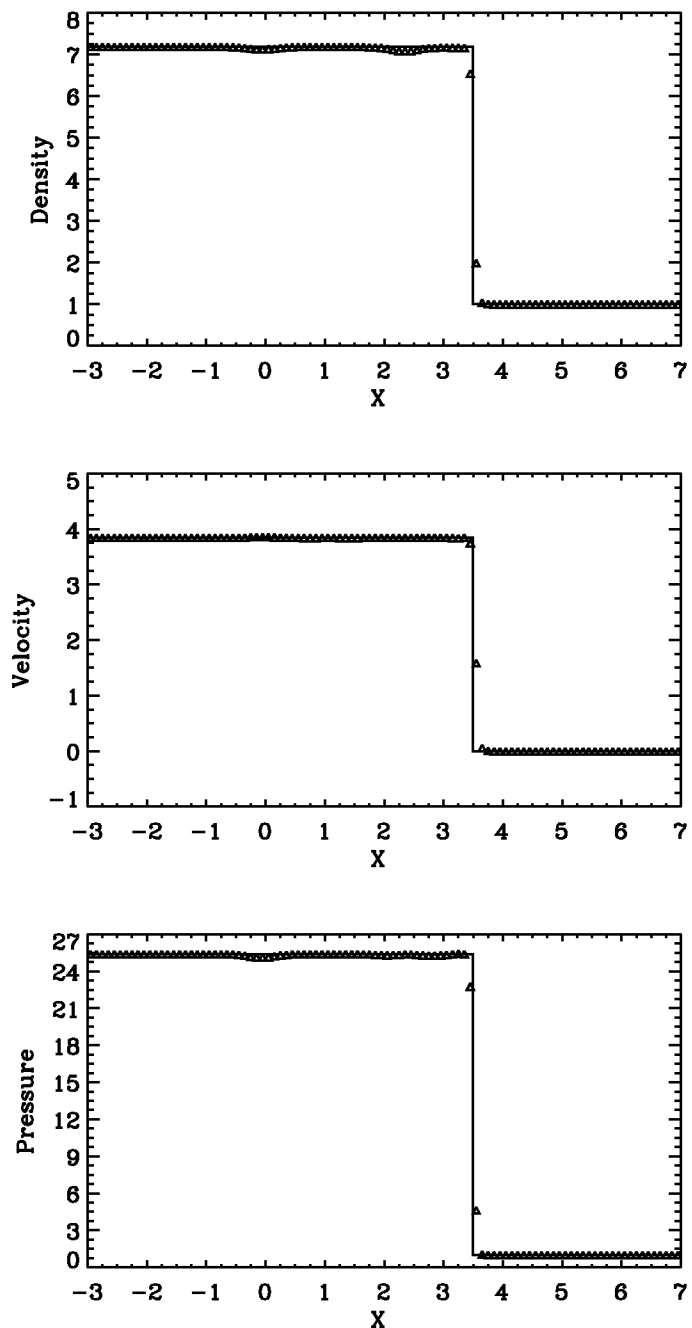


Figure 8: The CE/SE solution and the exact solution of the shock-wave merging problem ( $t = 1.1205$ ,  $\alpha = 2$ ).

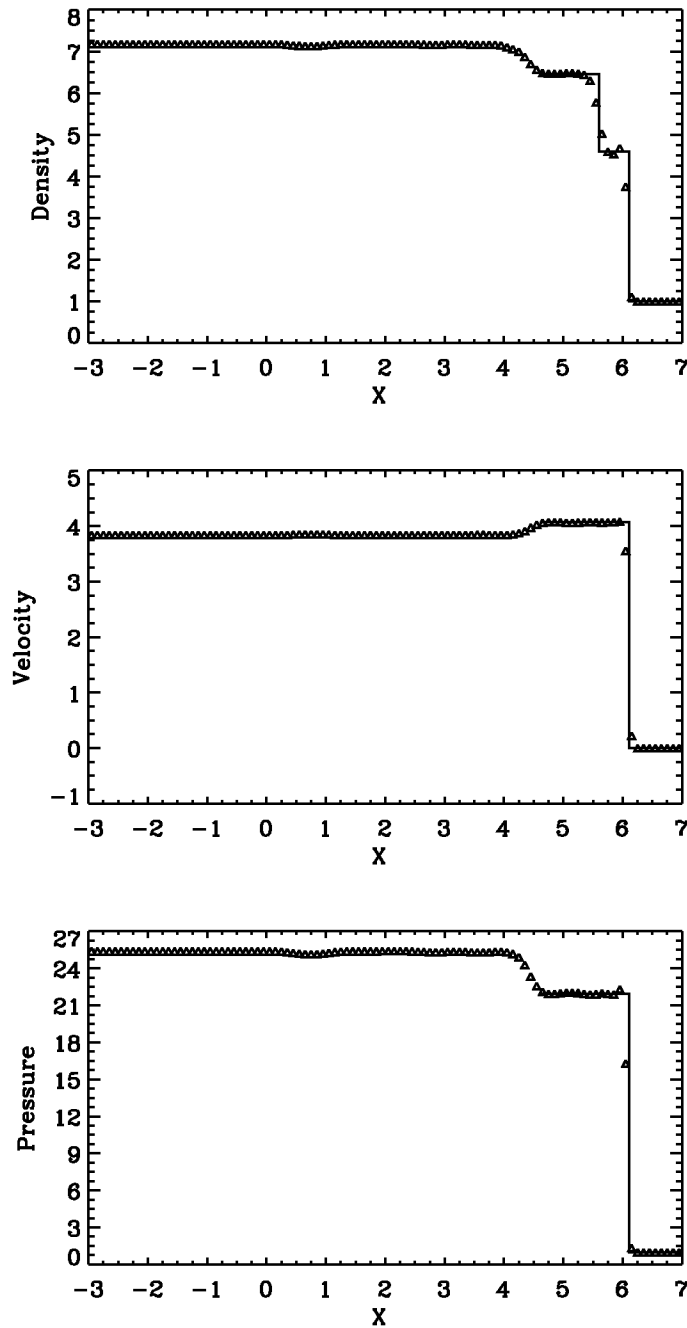


Figure 9: The CE/SE solution and the exact solution of the shock-wave merging problem ( $t = 1.62$ ,  $\alpha = 2$ ).

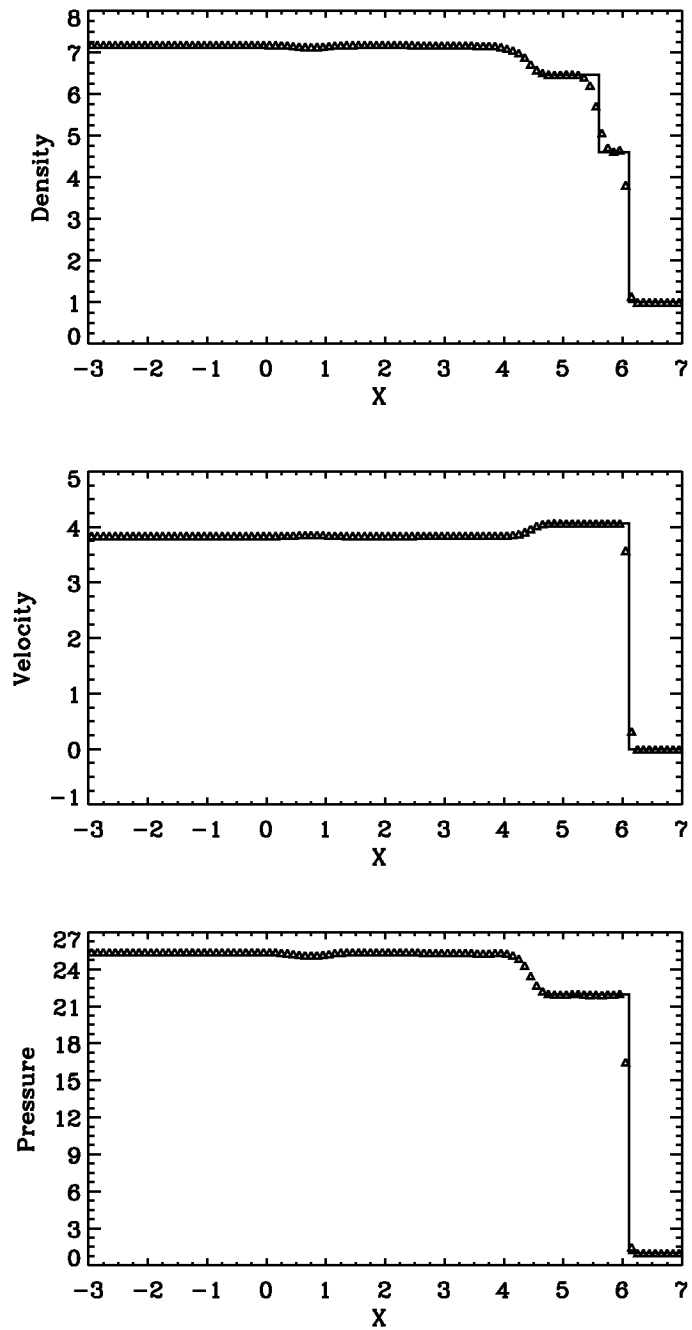


Figure 10: The CE/SE solution and the exact solution of the shock-wave merging problem ( $t = 1.62$ ,  $\alpha = 3$ ).

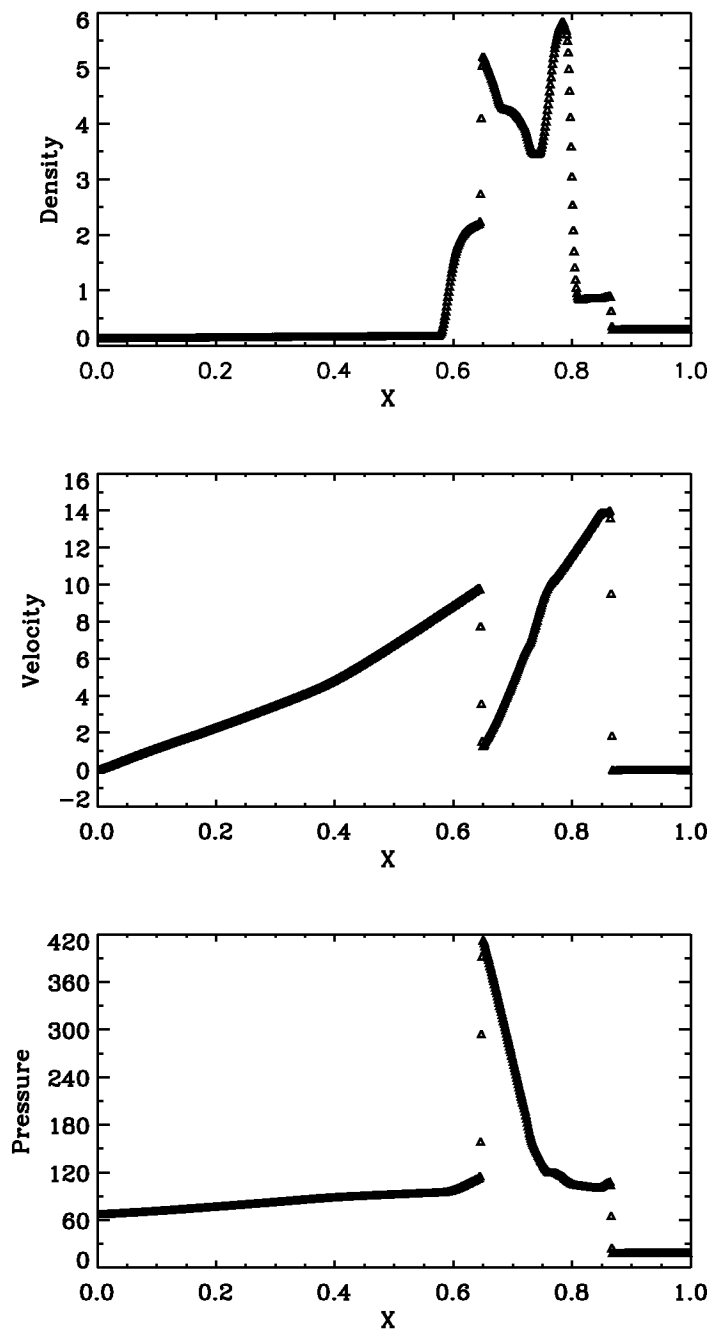


Figure 11: The CE/SE solution of the Woodward-Colella problem.

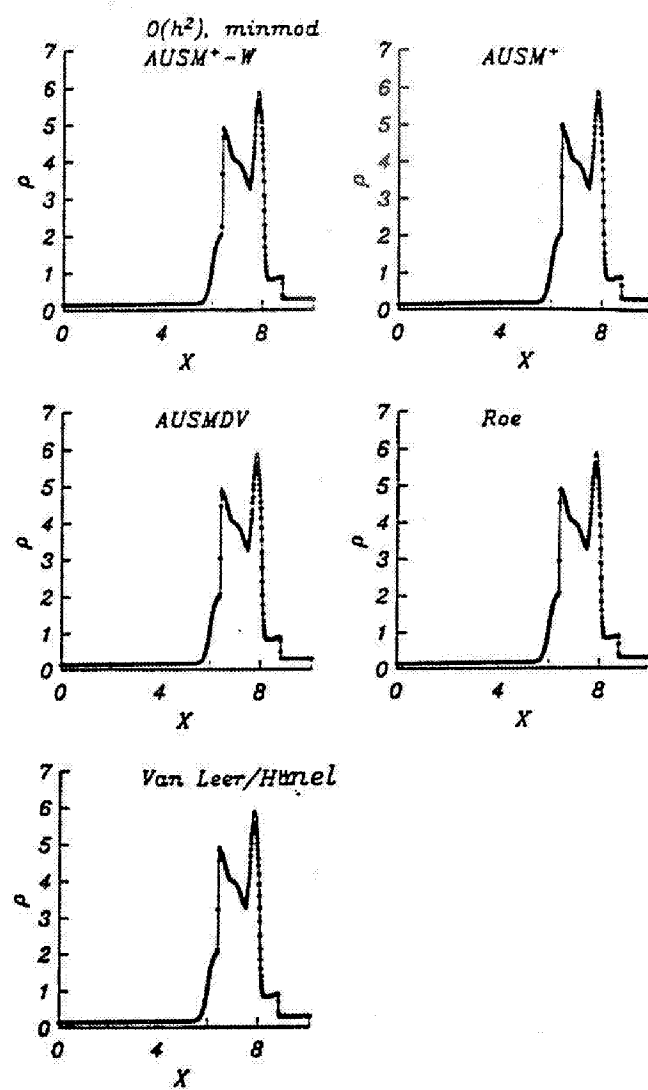
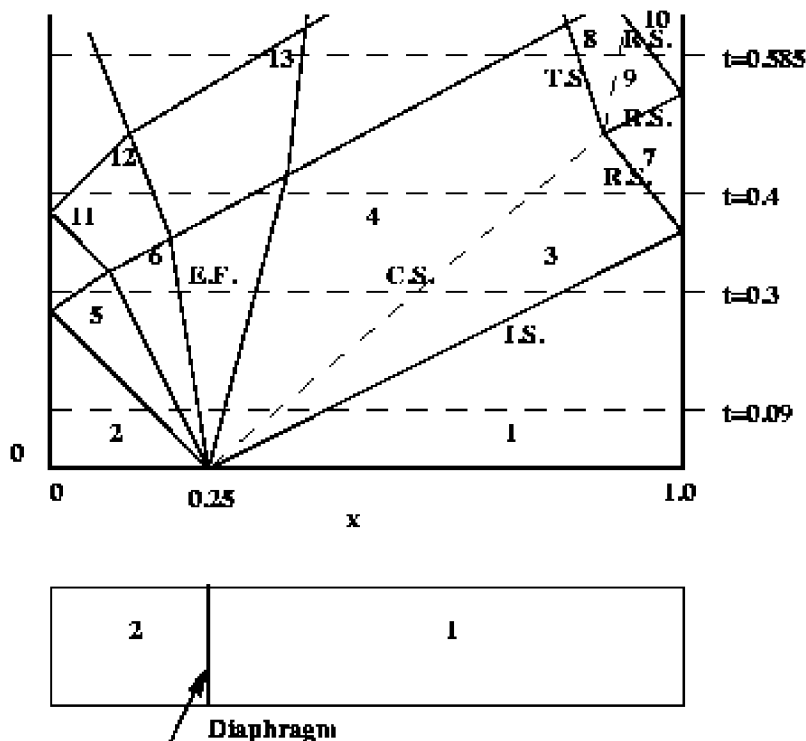


Figure 12: Upwind solutions of the Woodward-Colella problem.



<b>C.S.</b>	<b>Contact Surface</b>	<b>I.S.</b>	<b>Incident shock</b>
<b>E.F.</b>	<b>Expansion Fan</b>	<b>R.S.</b>	<b>Reflected Shock</b>
<b>T.S.</b>		<b>Transmitted Shock</b>	

Figure 13: Waves in a shock-tube with closed ends.

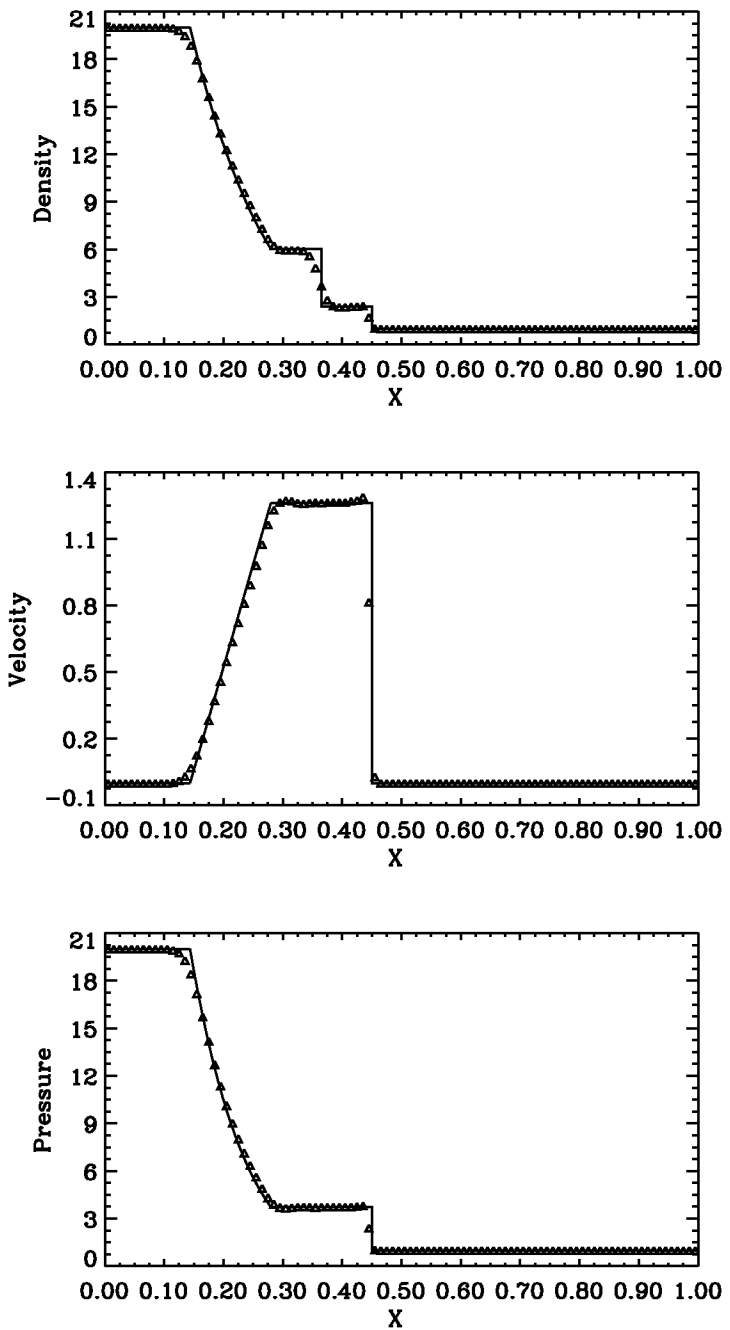


Figure 14: The CE/SE solution and the exact solution of the waves in a shock-tube with closed ends problem ( $t = 0.09$ ).

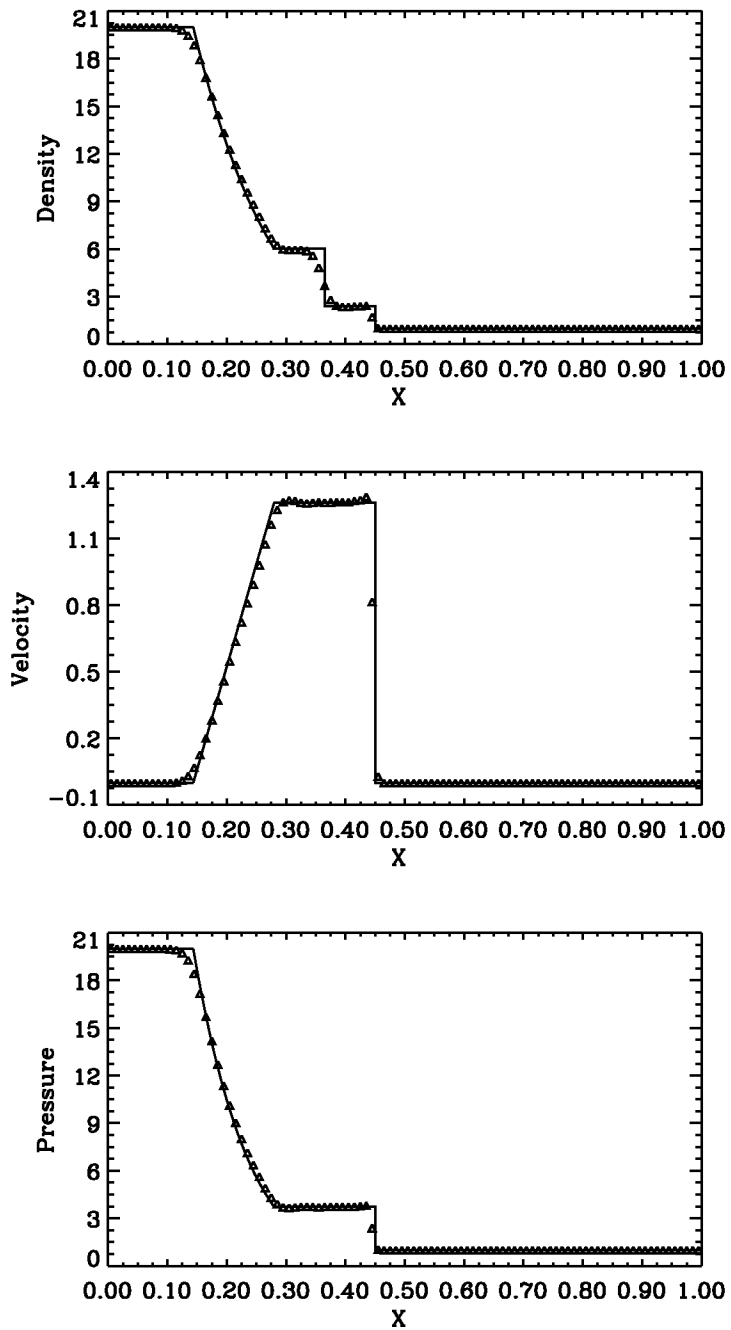


Figure 15: The CE/SE solution and the exact solution of the waves in a shock-tube with closed ends problem ( $t = 0.3$ ).

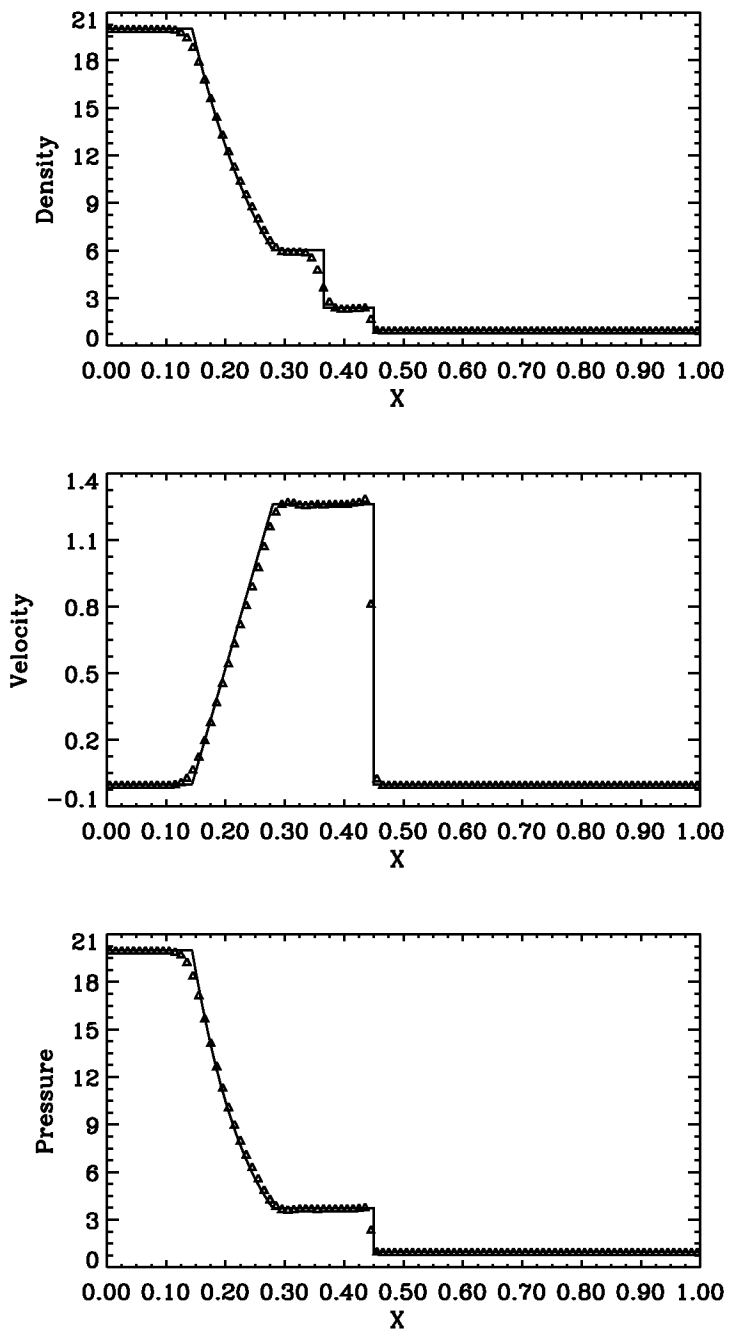


Figure 16: The CE/SE solution and the exact solution of the waves in a shock-tube with closed ends problem ( $t = 0.4$ ).

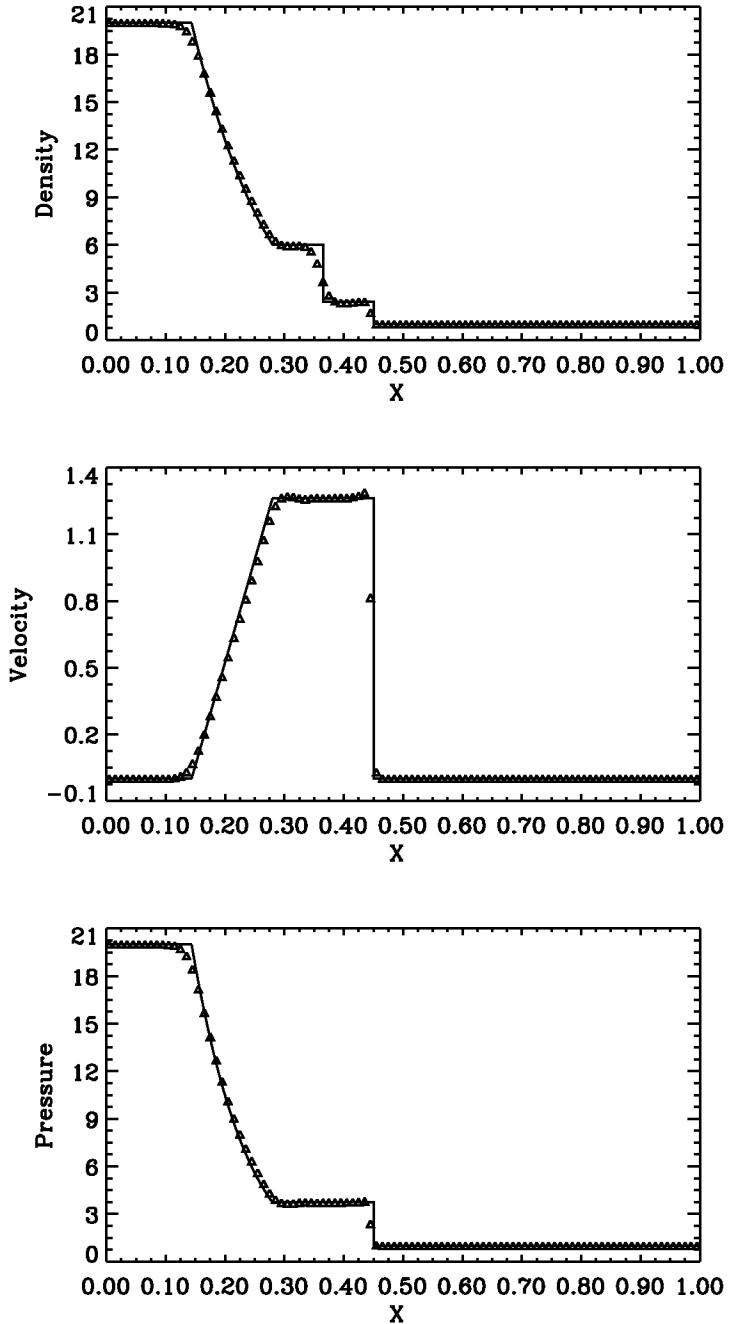


Figure 17: The CE/SE solution and the exact solution of the waves in a shock-tube with closed ends problem ( $t = 0.585$ ).

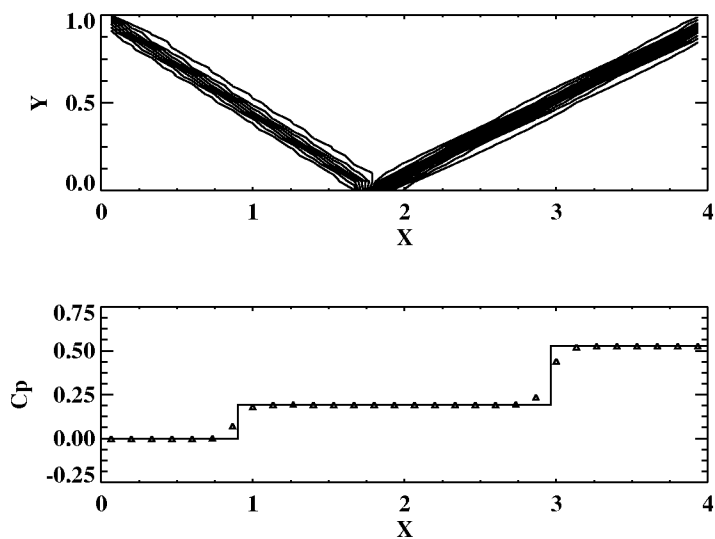


Figure 18: Pressure contours and pressure coefficient at  $y = 0.5$  of the oblique shock problem (60x20 mesh).

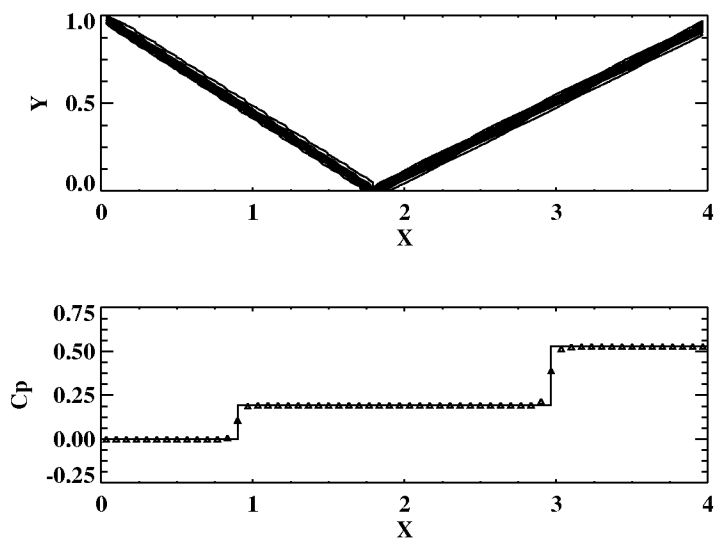


Figure 19: Pressure contours and pressure coefficient at  $y = 0.5$  of the oblique shock problem (120x40 mesh).

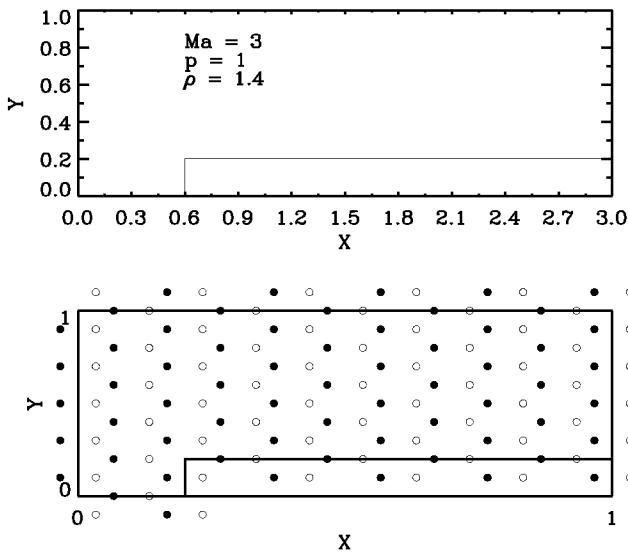


Figure 20: Geometry and Grid distribution of the 2D supersonic flow past a step problem.

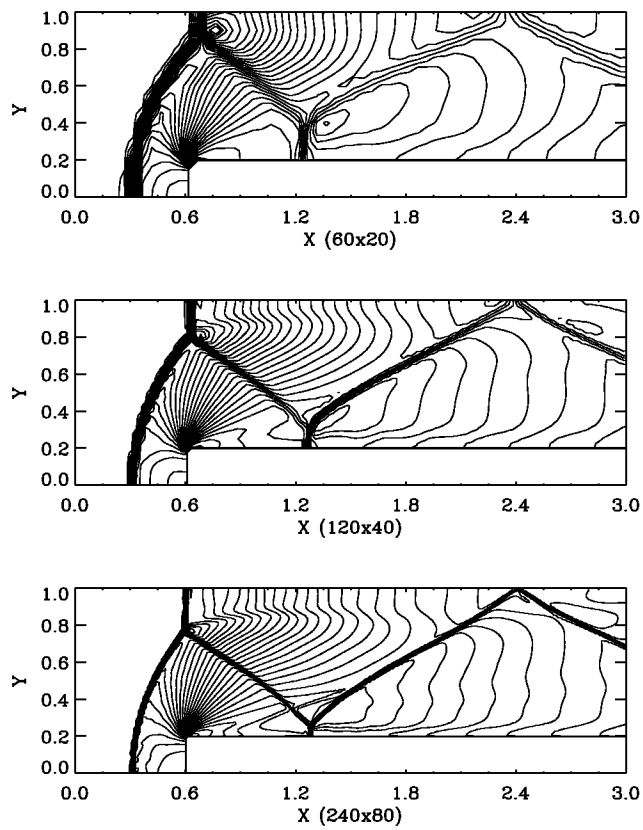


Figure 21: Density contours of the 2D supersonic flow past a step problem generated using 60x20, 120x40, and 240x80 meshes.

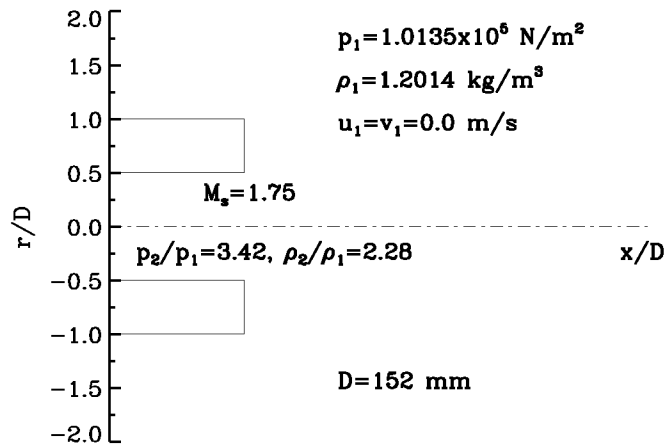


Figure 22: The initial conditions and geometry (cross section) of a cylindrical shock tube for the blast wave problem.

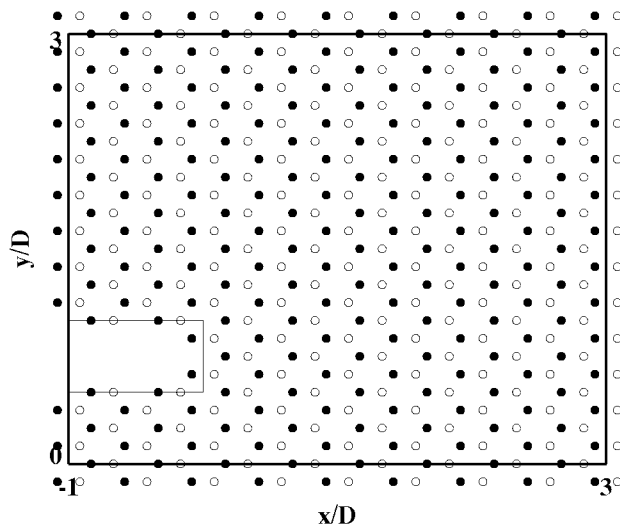


Figure 23: The computational domain and mesh-point distribution of the blast wave problem (planar-flow version).

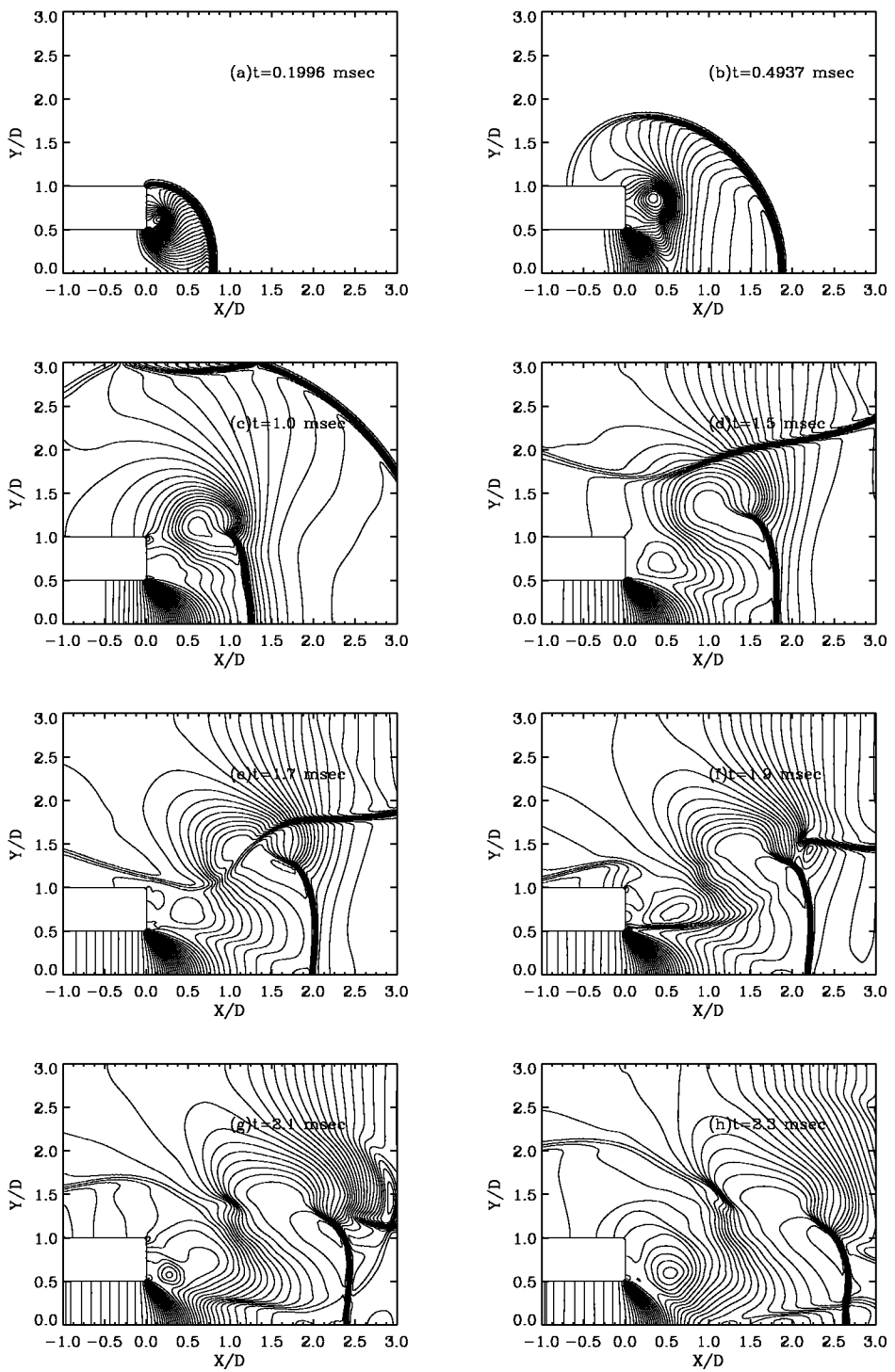


Figure 24: Pressure contours of the blast wave problem at eight different time levels.

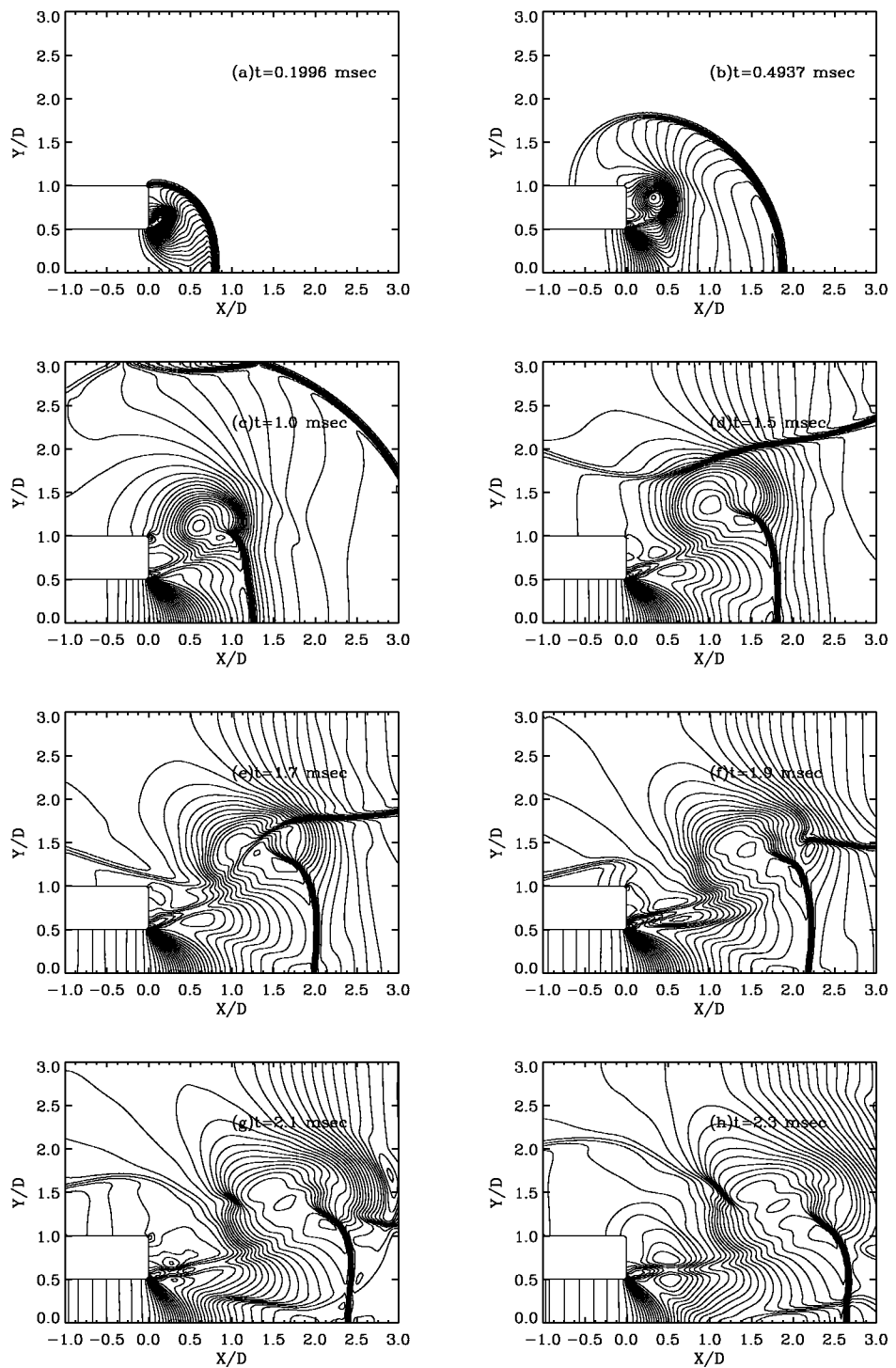


Figure 25: Density contours of the blast wave problem at eight different time levels.

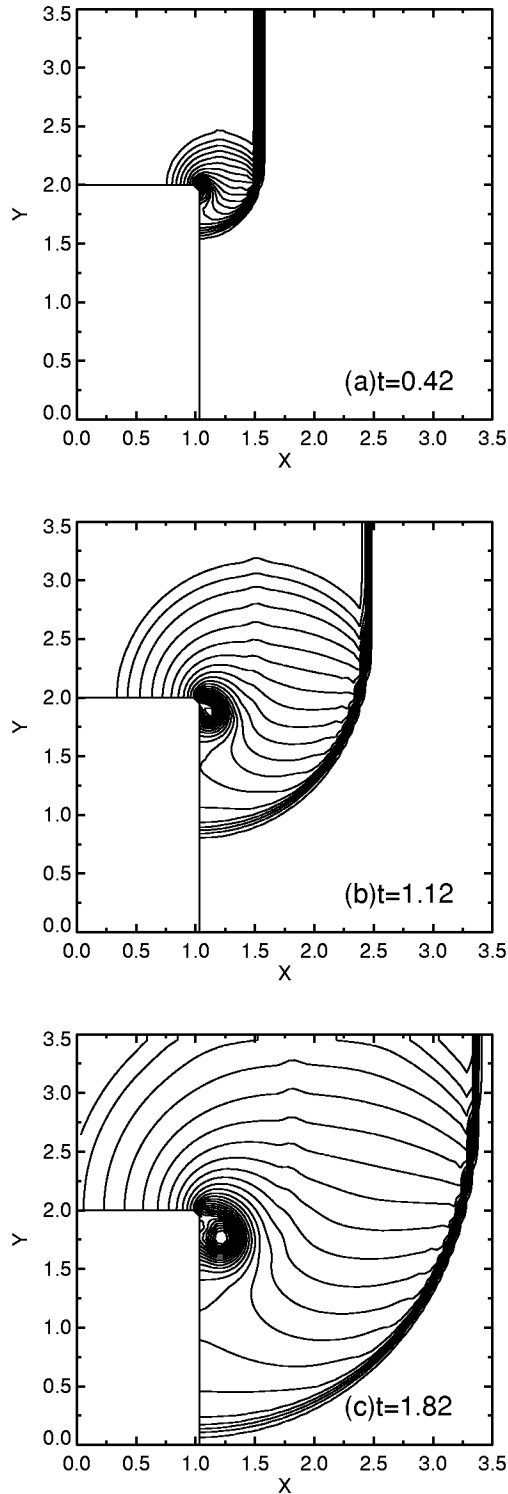


Figure 26: The computational domain and density contours at three different time levels of the diffraction of shock wave down a step problem (first case).

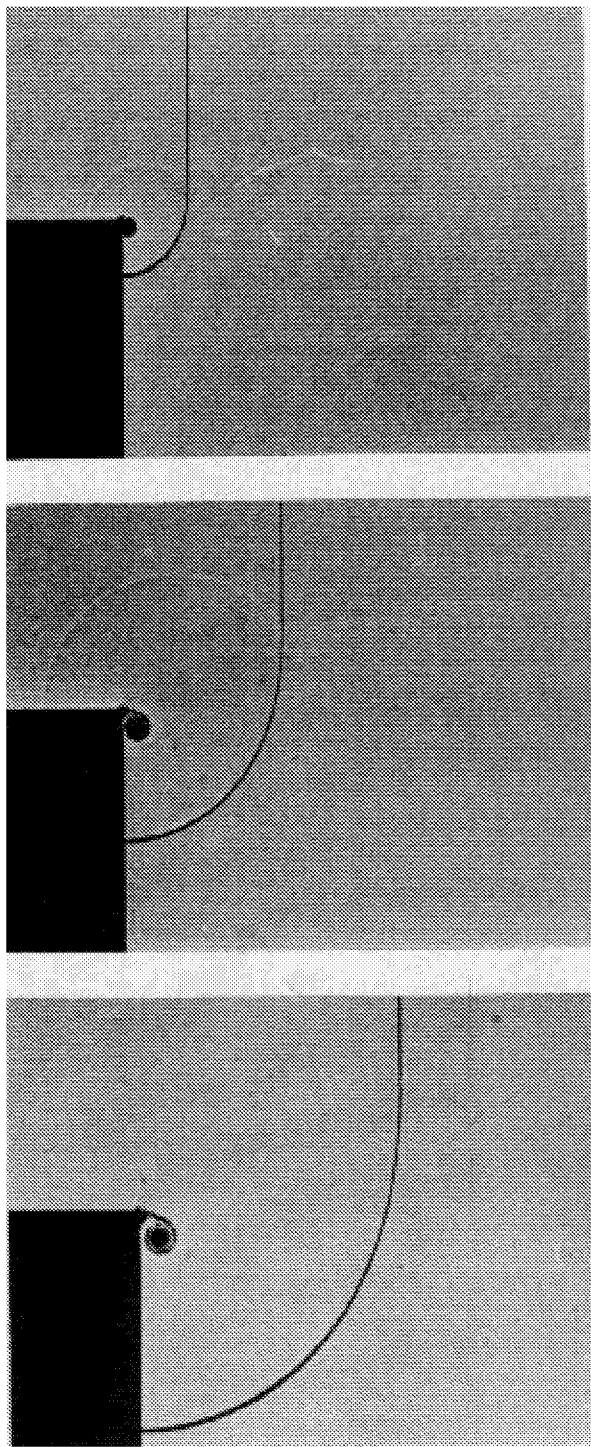


Figure 27: Experimental results of the diffraction of shock wave down a step problem (first case—three different time levels).

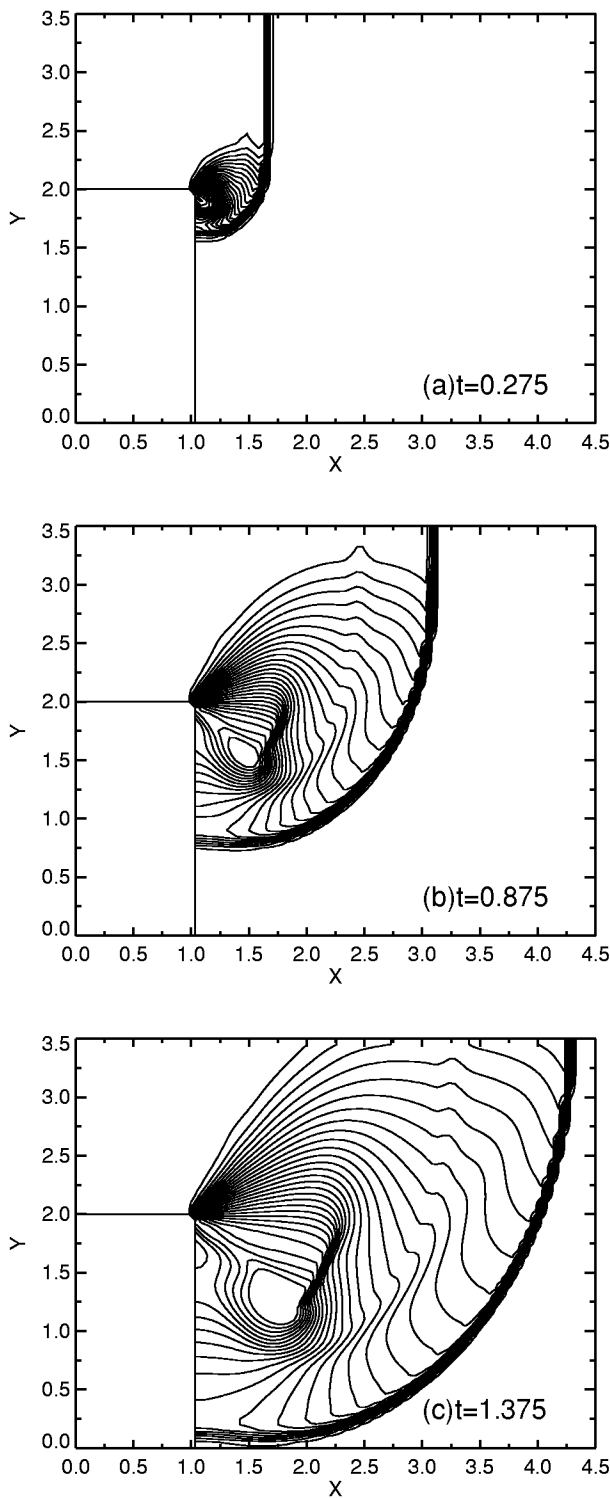


Figure 28: The computational domain and density contours at three different time levels of the diffraction of shock wave down a step problem (second case).

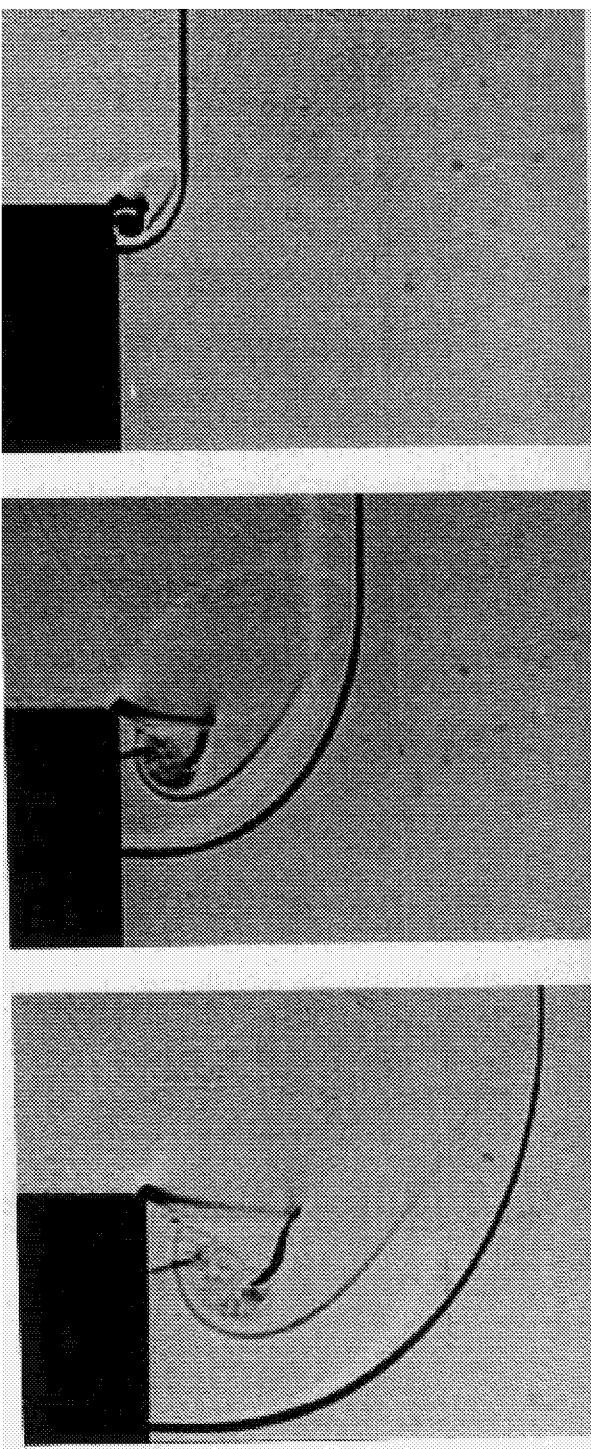


Figure 29: Experimental results of the diffraction of shock wave down a step problem (second case—three different time levels).

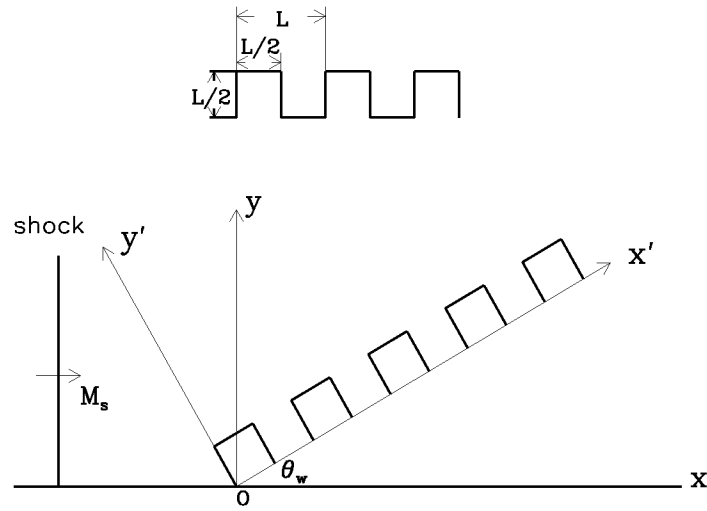


Figure 30: Shock moving past a wedge with a dust layer.

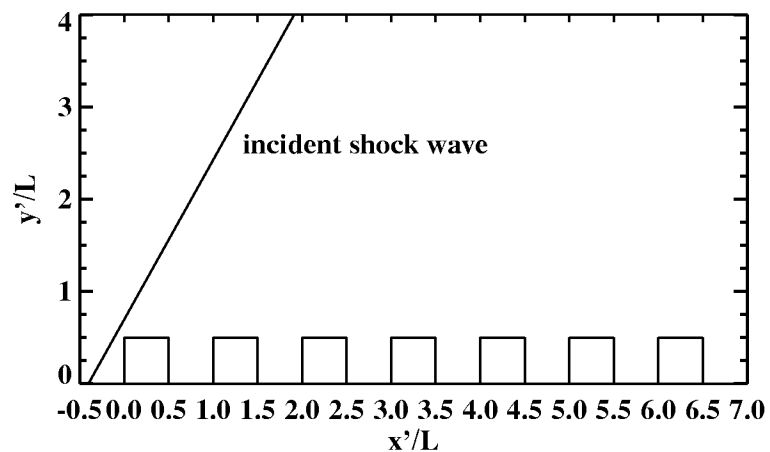


Figure 31: The computational domain of the dust layer problem.

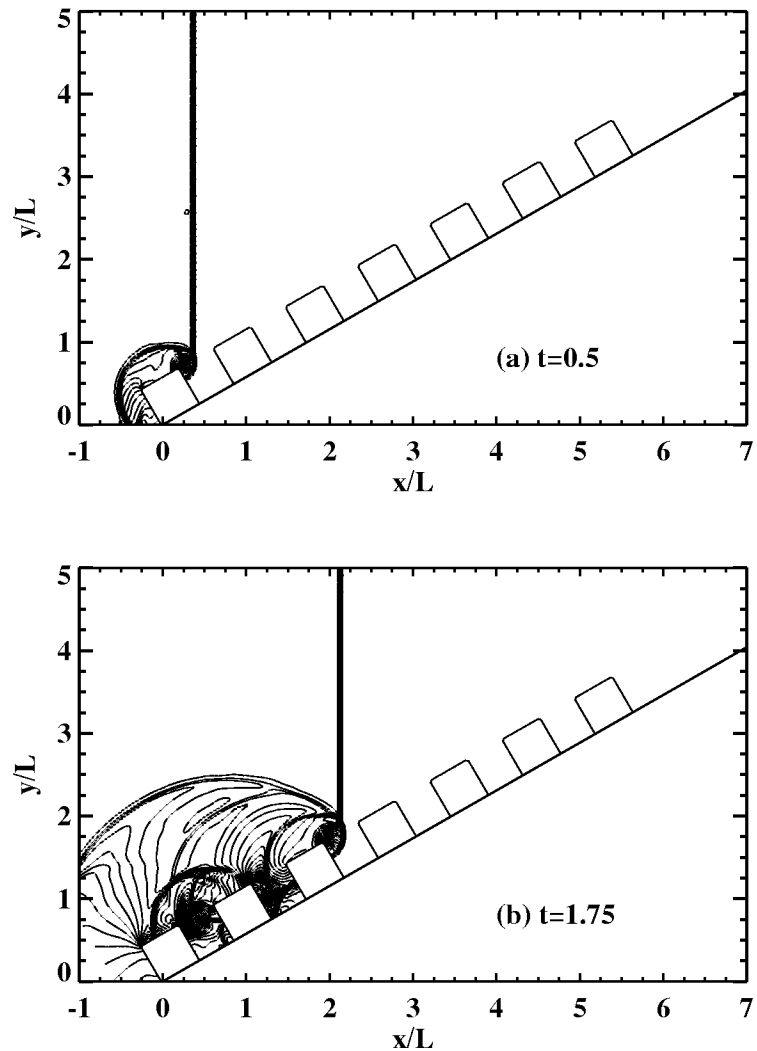


Figure 32: Density contours for the dust layer problem ( $\theta_W = 30^\circ$ ) at four different time levels. (a)  $t = 0.5$ , (b)  $t = 1.75$ , (c)  $t = 3$ , (d)  $t = 4$ .

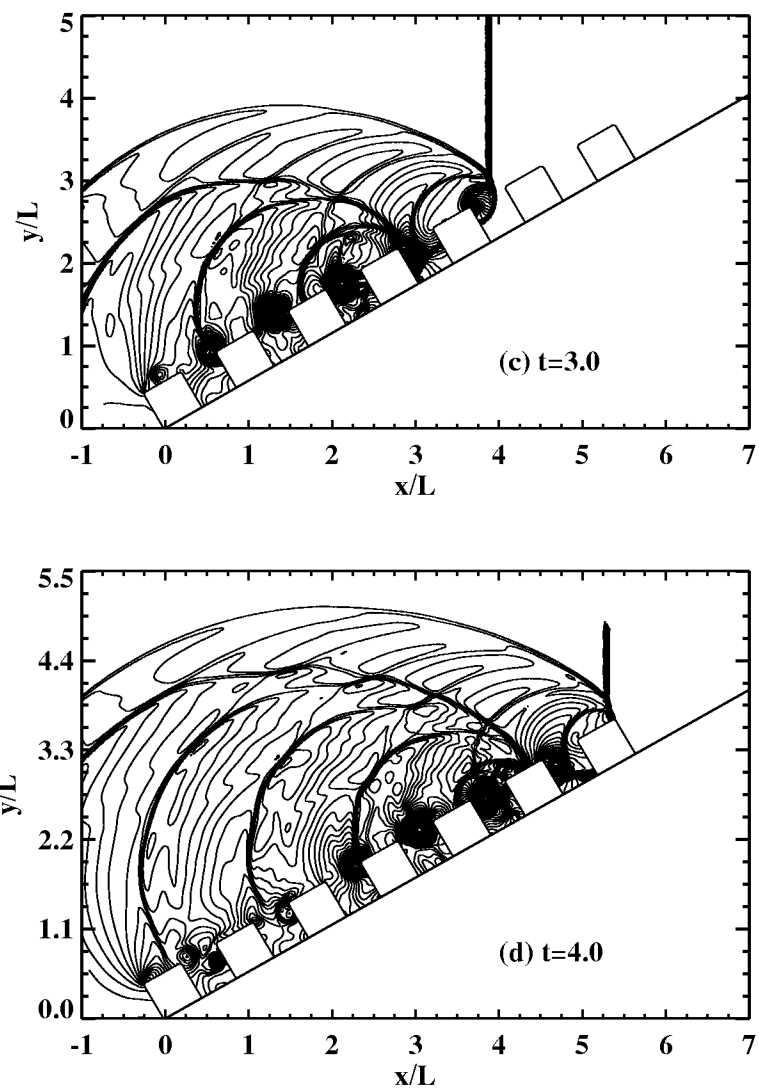


Figure 32: (continued)

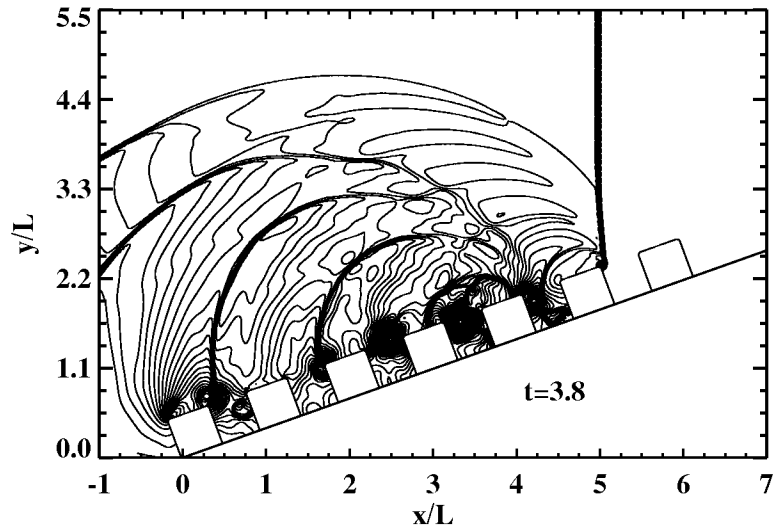


Figure 33: Density contours at  $t = 3.8$  for the dust layer problem ( $\theta_W = 20^\circ$ ).

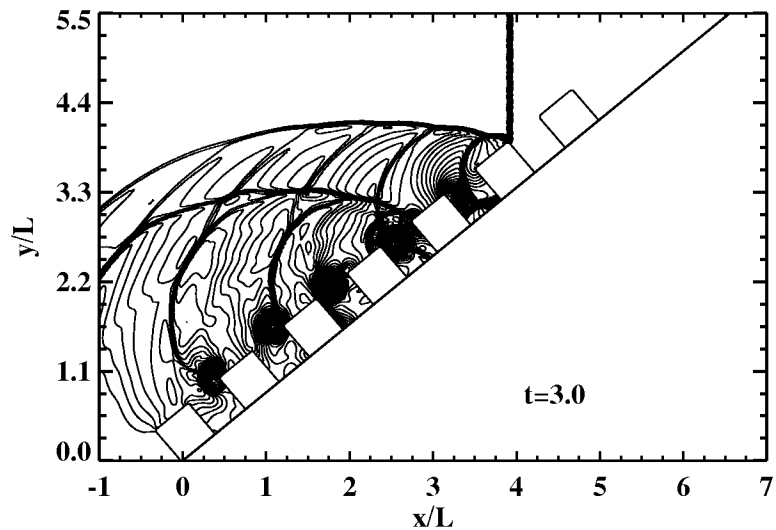


Figure 34: Density contours at  $t = 3.0$  for the dust layer problem ( $\theta_W = 40^\circ$ ).

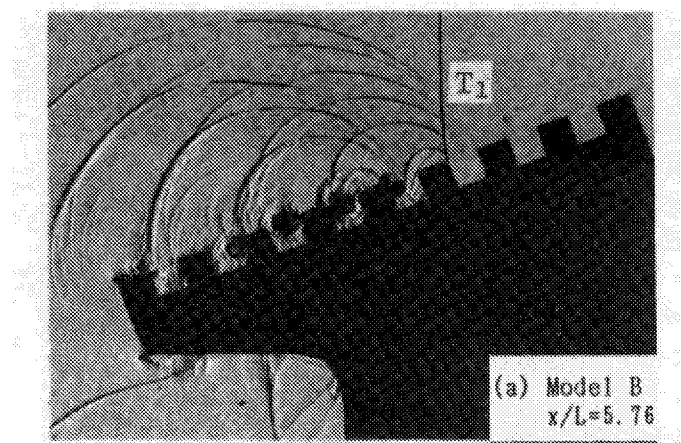


Figure 35: A schlieren photography for ( $\theta_W = 20^\circ$ ).

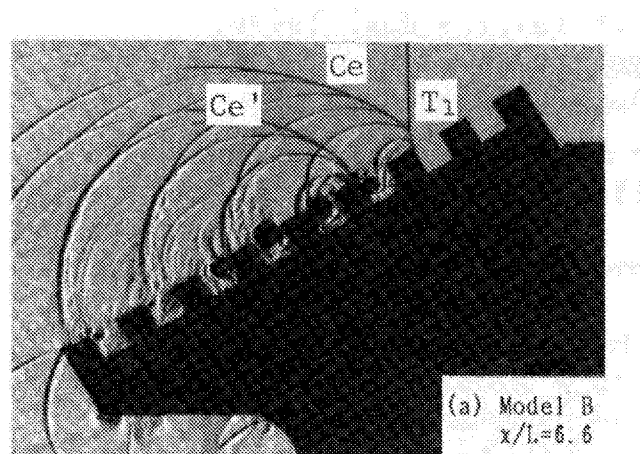


Figure 36: A schlieren photography for ( $\theta_W = 30^\circ$ ).

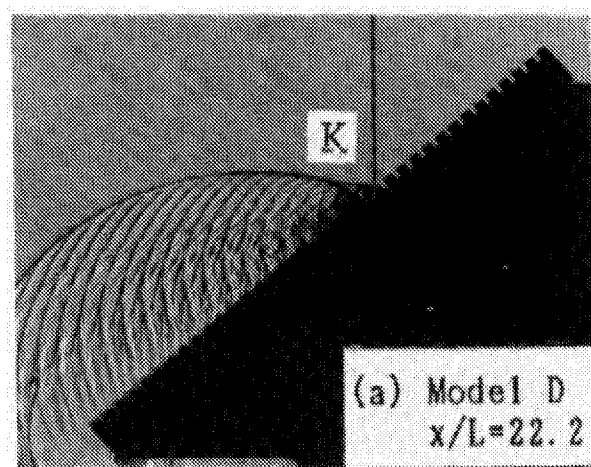


Figure 37: A schlieren photography for ( $\theta_W = 40^\circ$ ).

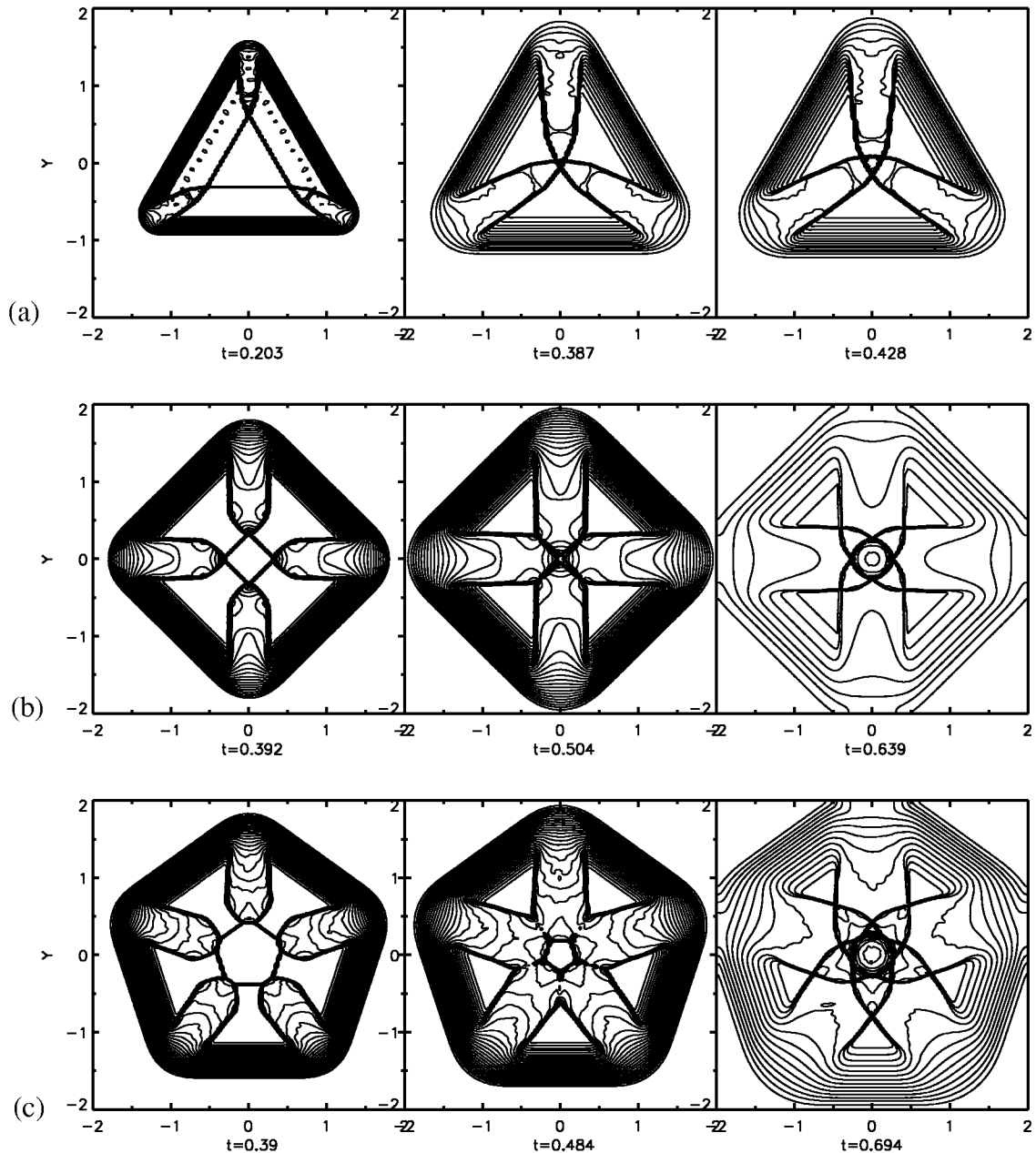


Figure 38: Pressure contours for implosion/explosion in a square box with different initial shock wave configurations.

- (a) an equilateral triangle.
- (b) a square.
- (c) a regular pentagon.

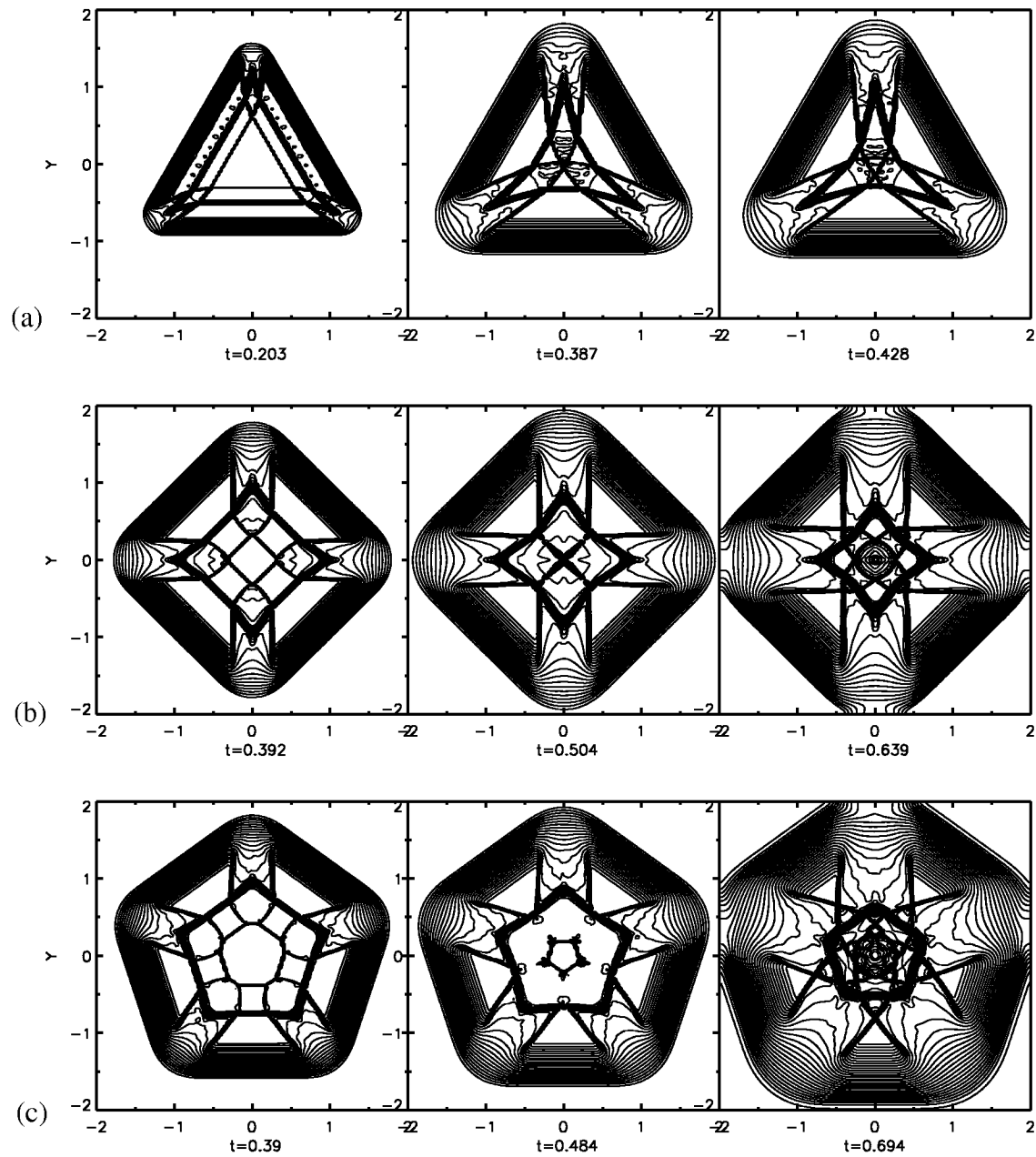


Figure 39: Density contours for implosion/explosion in a square box with different initial shock wave configurations.

- (a) an equilateral triangle.
- (b) a square.
- (c) a regular pentagon.

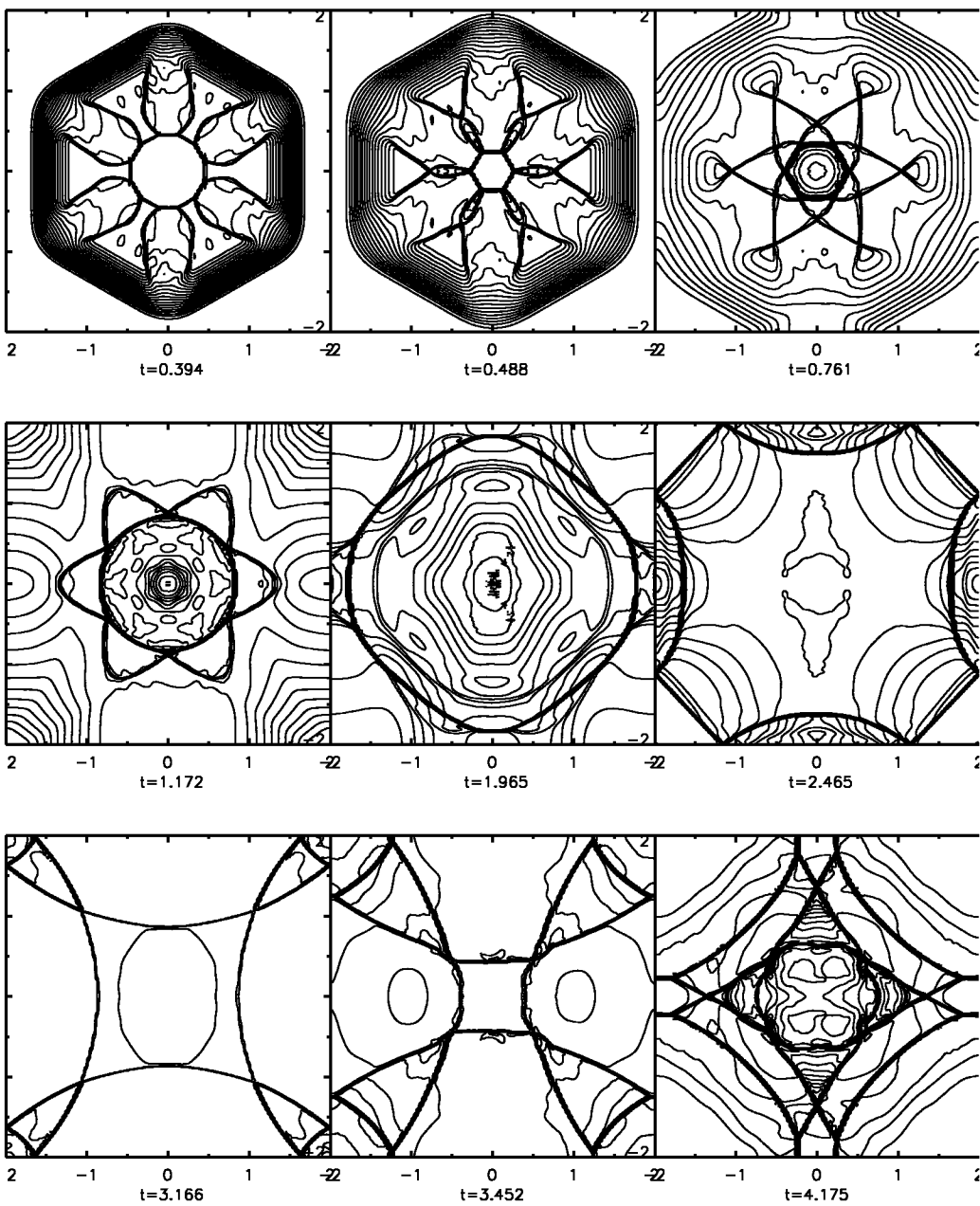


Figure 40: Pressure contours for implosion/explosion of a hexagonal shock in a square box.

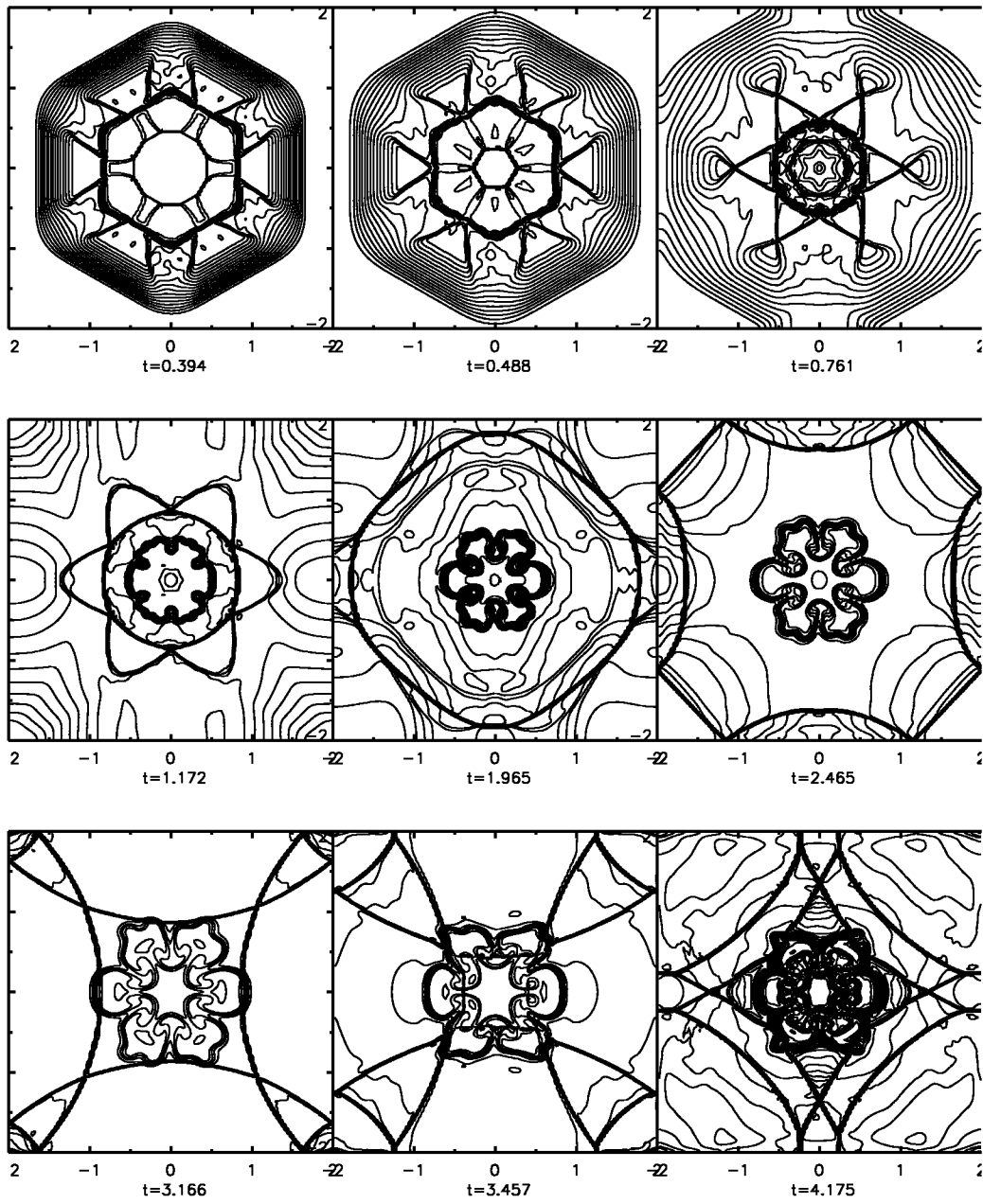


Figure 41: Density contours for implosion/explosion of a hexagonal shock in a square box.

REPORT DOCUMENTATION PAGE			Form Approved OMB No. 0704-0188
<p>Public reporting burden for this collection of information is estimated to average 1 hour per response, including the time for reviewing instructions, searching existing data sources, gathering and maintaining the data needed, and completing and reviewing the collection of information. Send comments regarding this burden estimate or any other aspect of this collection of information, including suggestions for reducing this burden, to Washington Headquarters Services, Directorate for Information Operations and Reports, 1215 Jefferson Davis Highway, Suite 1204, Arlington, VA 22202-4302, and to the Office of Management and Budget, Paperwork Reduction Project (0704-0188), Washington, DC 20503.</p>			
1. AGENCY USE ONLY (Leave blank)	2. REPORT DATE	3. REPORT TYPE AND DATES COVERED	
	December 1998	Technical Memorandum	
4. TITLE AND SUBTITLE		5. FUNDING NUMBERS	
The Space-Time Conservation Element and Solution Element Method—A New High-Resolution and Genuinely Multidimensional Paradigm for Solving Conservation Laws II. Numerical Simulation of Shock Waves and Contact Discontinuities		WU-538-03-11-00	
6. AUTHOR(S)			
Xiao-Yen Wang, Chuen-Yen Chow, and Sin-Chung Chang			
7. PERFORMING ORGANIZATION NAME(S) AND ADDRESS(ES)		8. PERFORMING ORGANIZATION REPORT NUMBER	
National Aeronautics and Space Administration Lewis Research Center Cleveland, Ohio 44135-3191		E-11457	
9. SPONSORING/MONITORING AGENCY NAME(S) AND ADDRESS(ES)		10. SPONSORING/MONITORING AGENCY REPORT NUMBER	
National Aeronautics and Space Administration Washington, DC 20546-0001		NASA TM—1998-208844	
11. SUPPLEMENTARY NOTES			
Xiao-Yen Wang, Department of Aerospace Engineering and Mechanics, University of Minnesota, Minneapolis, Minnesota 55455; Chuen-Yen Chow, Department of Aerospace Engineering and Science, University of Colorado at Boulder, Boulder, Colorado 80309-0429; Sin-Chung Chang, NASA Lewis Research Center. Responsible person, Sin-Chung Chang, organization code 5880, (216) 433-5874.			
12a. DISTRIBUTION/AVAILABILITY STATEMENT		12b. DISTRIBUTION CODE	
Unclassified - Unlimited Subject Categories: 34, 59, 61		Distribution: Nonstandard	
This publication is available from the NASA Center for AeroSpace Information, (301) 621-0390.			
13. ABSTRACT (Maximum 200 words)			
<p>Without resorting to special treatment for each individual test case, the 1D and 2D CE/SE shock-capturing schemes described in Part I are used to simulate flows involving phenomena such as shock waves, contact discontinuities, expansion waves and their interactions. Five 1D and six 2D problems are considered to examine the capability and robustness of these schemes. Despite their simple logical structures and low computational cost (for the 2D CE/SE shock-capturing scheme, the CPU time is about 2 <math>\mu</math>secs per mesh point per marching step on a Cray C90 machine), the numerical results, when compared with experimental data, exact solutions or numerical solutions by other methods, indicate that these schemes can accurately resolve shock and contact discontinuities consistently.</p>			
14. SUBJECT TERMS			15. NUMBER OF PAGES
Space-Time; Flux conservation; Conservation element; Solution element; Shocks; Contact discontinuities			60
			16. PRICE CODE
			A04
17. SECURITY CLASSIFICATION OF REPORT	18. SECURITY CLASSIFICATION OF THIS PAGE	19. SECURITY CLASSIFICATION OF ABSTRACT	20. LIMITATION OF ABSTRACT
Unclassified	Unclassified	Unclassified	